Neptune's Stratospheric Winds from Three Central Flash Occultations

Richard G. French

Astronomy Department, Wellesley College, Wellesley, Massachusetts 02481
E-mail: rfrench@wellesley.edu

Colleen A. McGhee

Astronomy Department, Cornell University, Ithaca, New York 14853

and

Bruno Sicardy

Observatorie de Paris–Institut Universitaire de France/Université Paris 6, 92195 Meudon Cédex, France

We present observations of three Neptune central flash events: the 20 August 1985 occultation of n39 from the European Southern Observatory (ESO), the 12 September 1988 occultation of N51 from Pic du Midi, and the 8 July 1989 occultation of N55 from ESO. From simultaneous fits to the three central flash lightcurves, we determine the shape of Neptune's limb, and show that winds near the 0.38-mbar level have decayed to about $\simeq 0.6 \pm 0.2$ times their strength at 100 mbar, assuming that the latitude-dependence of the stratospheric winds follows the zonal wind profile of L. A. Sromovsky *et al.* (1993, *Icarus* **105**, 110–141). From the measured decay of winds with height, we find that the average vertical shear in the zonal wind between 100 and 0.38 mbar is very close to the Voyager IRIS results for the 30- to 120-mbar region (B. J. Conrath *et al.*, 1989, *Science* **246**, 1454–1459), at the latitudes to which the central flashes are most sensitive. We also determine the shape of the limb at the 0.7-μbar level from the "half-light" points of the atmospheric immersion and emersion light curves of five stellar occultations by Neptune. The winds in this pressure regime have decayed to $\simeq 0.17$ times their strength at the 100-mbar level, and the vertical shear in the zonal wind as determined from the thermal wind equation and Voyager IRIS measurements extends essentially unchanged all the way up to the microbar level of the stratosphere. Alternatively, a simple oblate model fit to the planetary limb gives an oblateness of $\varepsilon = 0.0180 \pm 0.0010$ and an equatorial radius of $r_e = 25262.7 \pm 3.5$ km. The corresponding rotation period is 16.59 ± 0.92 h, quite similar to that of Neptune's deep interior (16.11 h). This near corotation suggests that there is some coupling between Neptune's interior and the upper stratosphere, even though the intervening atmosphere between the cloud deck and the stratosphere has strong retrograde flow. © 1998
Academic Press

1. INTRODUCTION

During the past two decades, Neptune's path in the sky has traversed dense star fields of the Milky Way, resulting in many high quality stellar occultations. Under rare circumstances, the star may appear to pass almost directly behind the center of Neptune. In this configuration, the planet's atmosphere acts like an enormous lens, and focusing by the nearly spherical limb produces a "central flash," or momentary brightening, during mid-occultation. Since the focal pattern of the atmospheric lens depends quite sensitively on the shape of the planetary limb, which is in turn affected by zonal winds, it is possible to determine the nature of planetary stratospheric winds from central flash observations. This technique has been applied to Titan (Hubbard *et al.* 1993) and to Saturn (Nicholson *et al.* 1995a), and here we extend the method to determine Neptune's stratospheric zonal wind profile from a joint analysis of three central flash occultations: the 20 August 1985 occultation of star n39, the 12 September 1988 occultation of N51, and the 7/8 July 1989 occultation of N55.

Neptune has extremely strong differential rotation at the cloud-top level, as determined from tracking of cloud features in Voyager 2 images (Sromovsky *et al.* 1993), and Voyager IRIS observations indicate that Neptune's zonal winds decay with height at the 30- to 120-mbar level (Conrath *et al.* 1989), as is the case for the other giant planets (Hanel *et al.* 1981, 1982, 1986, Flasar *et al.* 1987). However, the vertical extent of the differential rotation in Neptune's stratosphere has not previously been determined. Although the n39 event has been investigated by Lellouch *et al.* (1986) and Hubbard *et al.* (1987), they fitted simple

oblate limb models to the central flash lightcurves and did not attempt to determine the differential rotation of the atmosphere. By combining three central flashes with two additional multiple-station occultations, we have extended their results to determine the zonal wind profile of Neptune's stratosphere at the ~1-mbar regime probed by the central flash and in the ~1-μbar region sampled by the atmospheric occultations.

In Section 2, we summarize the central flash observations, and in Section 3 we determine the occultation geometry from fits of Neptune's limb to the times of disappearance and reappearance of the star behind the planet. We construct central flash models for the observations in Section 4, using the observed zonal wind profile from Voyager cloud motion studies as well as direct retrieval of the zonal winds from the central flash observations themselves. These results demonstrate that the winds decay with height, and in Section 5 we calculate the corresponding vertical shear in the zonal wind in the stratosphere. We fit an oblate limb model to the atmospheric occultation data and show that the winds in the microbar region of the atmosphere are nearly in corotation with the deep interior of the planet. Finally, in Section 6, we present our conclusions.

2. OBSERVATIONS

Figure 1 shows the occultation tracks for the three central flash occultations, and the observations are shown in Fig. 2, with the entire lightcurve for each event at left and the higher resolution central flash lightcurve at right. In the case of the N51 event, the observed signal reached 40% of the full signal from the unoccluded star, with appreciable but more moderate central flashes for the other two occultations.

2.1. The 20 August 1985 Occultation of n39

The Neptune occultation of this very bright ($K = 6.4$) star, designated n39 on an unpublished prediction list of P. Nicholson, was observed simultaneously from ESO and CTIO in Chile and featured a very prominent central flash. Lellouch *et al.* (1986) and Hubbard *et al.* (1987) described the observations and their determinations of the oblateness of Neptune's limb from model fits to the flash profiles. The detailed differences between the CTIO and ESO lightcurves were studied by Hubbard *et al.* (1988) to determine properties of scintillation by Neptune's atmosphere, but these subtle differences are not essential for our present purposes, and we have used only the ESO data for the n39 event. The central flash is characterized by a sharp, symmetric intensity peak, reaching 20% of the full stellar intensity at about 5.92 UT (Fig. 2), rising above a broad, asymmetric pedestal of $\simeq$10 min duration, corresponding to $\simeq$6000 km along the occultation track.
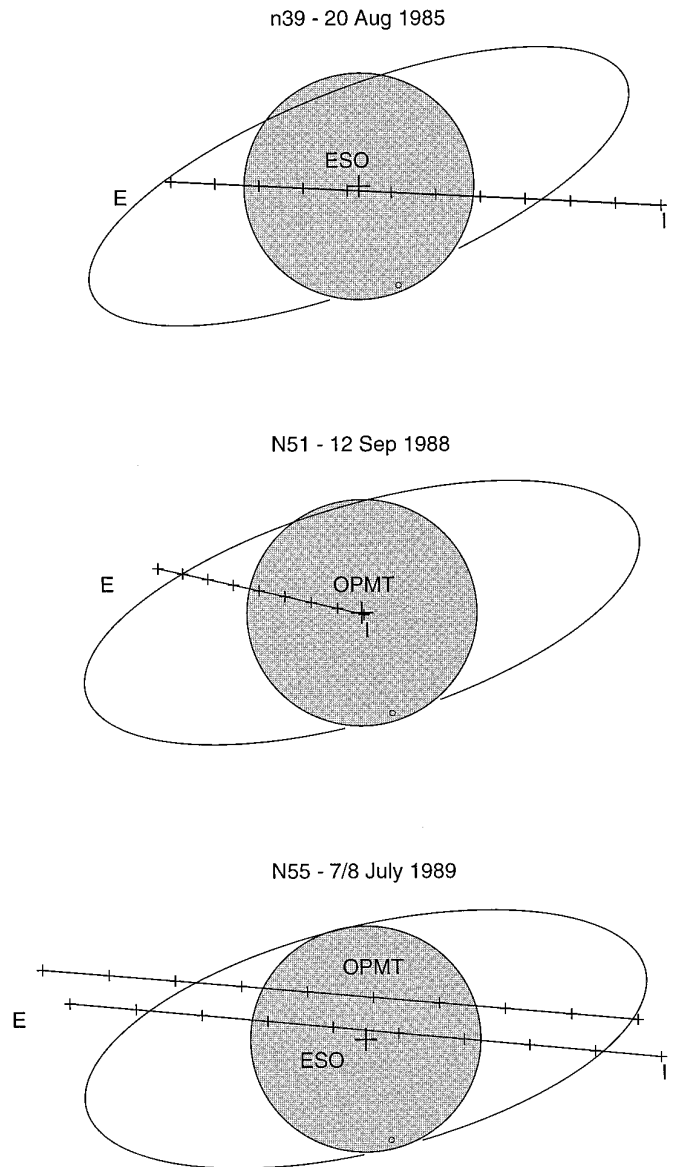
FIG. 1. The apparent path of the occultation star relative to Neptune is shown for observers of the n39, N51, and N55 occultations. The Adams ring is included to illustrate the orientation of Neptune's pole and the declination of Earth at the time of the occultation. For each event, a central flash was observed along the chord passing closest to the geometric center of the planet (marked by a "+"). Tick marks along the paths are 15, 30, and 10 min apart for the n39, N51, and N55 events, respectively.

2.2. The 12 September 1988 Occultation of N51

The occultation of N51, from the prediction list of Mink and Klemola (1985), was exceptional because of the star's brightness ($I = 11.4$, $K = 6.8$) and the low sky-plane velocity of the event ($v = 3.2$ km s^{-1}). At the same time, however, Neptune was at very high airmass during the observations, which somewhat degraded the quality of the lightcurves (see Sicardy *et al.* (1991) and Roques *et al.* (1994) for additional details). The observations were carried out using
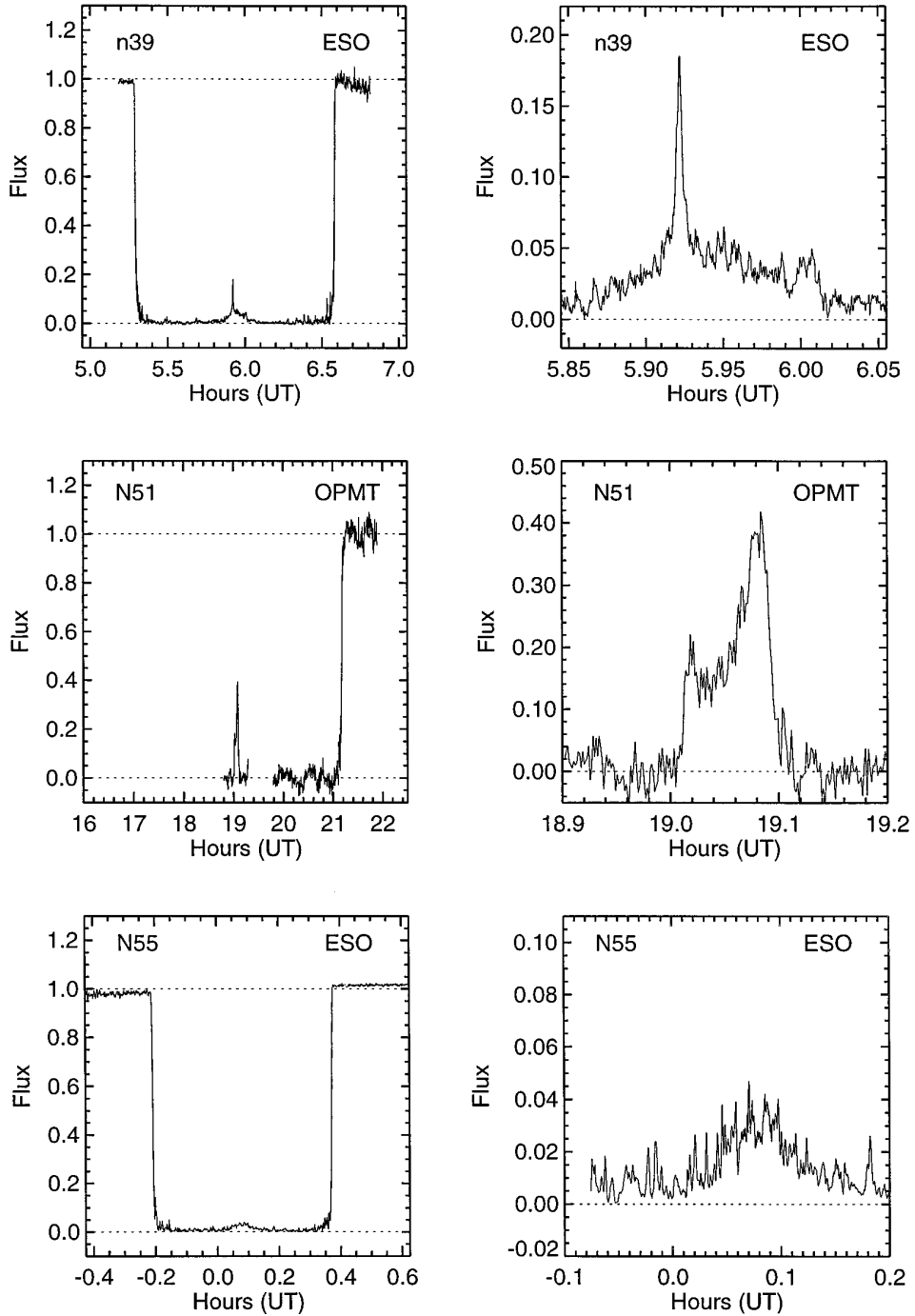
FIG. 2. (Top row) The 20 August 1985 occultation of n39 as observed from ESO, with the entire lightcurve shown at left at a time resolution of 5 s, and an expanded view at right of the central flash region at 2 s resolution. (Middle row) The 12 September 1988 occultation of N51 as observed from Pic du Midi (OPMT). On the left is the normalized lightcurve for the central flash and atmospheric emersion, at 15 s resolution, and at right is the central flash at 5 s resolution. (Bottom row) Lightcurve for the 8 July 1989 occultation of N55 as observed from ESO at 5 s resolution (left) and the central flash region at 2 s resolution (right).

a two-channel GaAs aperture photometer on the 2-m Pic du Midi telescope. The signal channel, centered at the 0.89-μm methane band, was sensitive to the star, and a control channel, centered at 0.75 μm, was sensitive primar-

ily to Neptune. Observations began during twilight, after atmospheric immersion had already taken place. To obtain a normalized lightcurve, the signal channel at full resolution (20 Hz) was divided by the control channel, averaged

over 5 s to suppress photon noise.[1] This resulted in a smoother lightcurve, to which fourth-order polynomials were fitted. For the data after atmospheric emersion, the polynomial was divided by a constant factor so that it connected smoothly with the fitted polynomial before emersion. After division by the polynomials and normalization by the full stellar intensity, the final lightcurve shown in Fig. 2 was obtained. The central flash lasted for about 10 min ($\simeq$2000 km along the occultation track), with abrupt, asymmetric edges reaching 20% intensity at the onset and a full 40% at the end of the central flash.

2.3. The 8 July 1989 Occultation of N55

The central flash from the occultation of N55 (Mink and Klemola 1985) was observed from ESO under good weather conditions, and observations along a more northerly chord were obtained from Pic du Midi (OPMT). Further details of the observations are presented by Sicardy *et al.* (1991). The ESO 2.2-m data of this very bright infrared source ($K = 5.5$ and $I \sim 7$) have excellent SNR, and Fig. 2 shows the atmospheric immersion and emersion lightcurves and an extended low-amplitude central flash during mid-occultation.

3. ASTROMETRY

The detailed structure of a central flash lightcurve depends quite sensitively on the location of the observer's path across the planetary shadow. Consequently, it is important to determine that the occultation geometry as precisely as possible. We adopt the sky-plane formalism as described in Appendix A of French *et al.* (1993), where we let f and g be the instantaneous apparent east and north sky plane positions of the star, respectively, measured from the predicted center of the planet on the sky as given by the planetary ephemeris. The predicted occultation chord for a given observer is thus the apparent path of the star relative to the ephemeris position of the planet, given by $f(t)$ and $g(t)$. Because of the large a priori uncertainty in the relative positions of the occulted star and the planet, we must determine the true occultation geometry from the observations themselves. We assume that the *actual* planet position relative to the star in the sky plane is offset from the ephemeris value by (f_0, g_0). For the purpose of determining f_0 and g_0, the fundamental observations are the sky-plane coordinates of the "half-light" times, $t_{1/2}$, ob-

tained from fits of an isothermal atmosphere model to the available immersion and emersion occultation data. For a single-station occultation, the half-light times provide two degrees of freedom from which f_0 and g_0 may be found, but one must assume a particular shape of the projected planetary limb. In the present case, we have several multiple-station occultations, from which we can determine the ephemeris corrections f_0 and g_0 for each occultation *and* the best fitting limb shape.

The shape of Neptune's stratosphere has been investigated in this fashion, using the 7 April 1968 occultation of BD–17° 4388 (henceforth designated as n1968; Kovalevsky and Link 1969, Freeman and Lyngå 1970) and the 15 June 1983 occultation of N30 (Hubbard *et al.* 1985, French *et al.* 1985). These investigators assumed an elliptical figure for the planet, and determined the oblateness of Neptune that gave the best fit to the observations. We have extended this approach by including atmospheric half-light times for the central flash occultations n39, N51, and N55. To provide a basis of comparison with earlier results, we have computed the best-fitting elliptical limb model, but we also allow for the possibility of differential rotation when calculating the planetary figure. We used the JPL DE-130 planetary ephemeris (Standish 1990, Standish *et al.* 1992) and the B1950.0 star positions as given in Table I to compute the sky-plane coordinates of the half-light times given in Table II. The apparent aspect of the planet at the time of each occultation is defined by the declination of the Earth, B, and the position angle of the projected rotation axis of Neptune, P, measured counterclockwise from apparent north, as given in Table I. We used the Jacobson *et al.* (1990) post-Voyager model for Neptune's pole direction, which takes into account the Triton-induced precession, as discussed by Nicholson *et al.* (1995b).

For consistency with our analysis of the central flash events, to be described below, we adopted a simple model for the rotation figure of Neptune. Cloud motion studies (Hammel *et al.* 1989, Limaye and Sromovsky 1991, Sromovsky *et al.* 1993) have shown that Neptune has a strong retrograde equatorial jet and north–south symmetry in the zonal wind (Limaye and Sromovsky 1991), although Voyager observations are limited at some latitudes because of the fly-by trajectory. There seems to be measurable variability about the mean flow, but in the absence of any more detailed information on Neptune's cloud motions at the times of the occultations, we have adopted the Sromovsky *et al.* (1993) fourth-order polynomial fit in latitude ϕ to cloud motions from Voyager images (see Appendix A, Sromovsky *et al.* 1993) as a reasonable point of departure:[2]

---

[1] Although Neptune's near-IR brightness is known to vary due to the evolution and transit of bright cloud features across a dark absorbing background, the central flash has a much larger amplitude and is much more abrupt than any reported variations due to clouds (see Baines *et al.* (1995) for a review). There are no short-term variations in Neptune's brightness in the 0.75-μm reference signal near the time of the central flash, nor in the methane channel at times away from the central flash. We therefore consider it unlikely that brightness variations due to cloud variability are contaminating the central flash light curve.

[2] These measurements apply to a height of 50–75 km above the global mean cloud deck (Limaye and Stromovsky 1991), which itself is at the $\sim$3-bar level (Smith *et al.* 1989). From Fig. 9 of Smith *et al.* (1989), we estimate the pressure level of the measured clouds to be at $p_{cloud} \simeq$ 100 mbar.

TABLE I
Elliptical Fit to Neptune's Limb

Star	Date	N^a	$\alpha(1950.0)$	$\delta(1950.0)$	$B(°)$	$P(°)^b$	$f_0(km)^c$	$g_0(km)^c$
BD—17°4388 (n1968)	1968 Apr. 7	6	$15^h\ 35^m\ 50.462^s$	$-17°\ 30'\ 7.94''$	-5.3807	41.7045	-11636.6 ± 15.2	2187.0 ± 32.6
N30	1983 June 15	11	$17^h\ 49^m\ 12.291^s$	$-22°\ 8'\ 59.78''$	-18.8404	23.7048	3659.5 ± 7.4	-1910.8 ± 14.7
n39	1985 Aug. 20	12	$18^h\ 2^m\ 7.186^s$	$-22°\ 18'\ 10.02''$	-19.8544	21.4895	9774.1 ± 4.0	-5509.4 ± 22.1
N51	1988 Sept. 12	1	$18^h\ 29^m\ 46.733^s$	$-22°\ 18'\ 13.14''$	-21.9600	16.5486	3872.7 ± 11.0	$(-750)^d$
N55	1989 July 8	6	$18^h\ 44^m\ 31.526^s$	$-22°\ 6'\ 32.61''$	-23.0543	13.8138	1618.3 ± 5.2	-1246.5 ± 21.6

Half-light r_e (km) $(25158.7 + 104) = 25262.7 \pm 3.5^e$ Oblateness $\varepsilon = 0.0180 \pm 0.0010$

[a] Number of half-light measurements for each occultation used in limb fit.

[b] Position angle of Neptune's pole, measured counterclockwise from apparent north.

[c] (f_0, g_0) are east and north offsets between the observed and predicted location of the planet in the sky plane relative to the star at the time of the occultation, measured in apparent coordinates.

[d] The N51 ephemeris offsets f_0 and g_0 are not uniquely determined by the fit, since only one half-light measurement exists for this occultation.

[e] The best-fitting equatorial radius to the sky plane points is augmented by 104 km to correct for general relativistic bending and refraction by Neptune's atmosphere.

$$u_{\text{Sromovsky}}(\phi) = k_1 + k_2\phi^2 + k_3\phi^4$$
$$= -389.0 + 0.188\phi^2 - 1.2 \times 10^{-5}\ \phi^4. \quad (1)$$

This representation of the zonal wind implies an infinite rotation speed at the poles, and we applied a cosine taper at high latitudes ($|\phi| > \phi_{\max} = 75°$) to force the winds to vanish at the poles:

$$T(u(\phi), \phi_{\max} > 0) =$$

$$\begin{cases} u(-\phi_{\max}) \cos[90(\phi + \phi_{\max})/(90 - \phi_{\max})] & \phi \leq -\phi_{\max} \\ u(\phi) & |\phi| < \phi_{\max} \\ u(\phi_{\max}) \cos[90(\phi - \phi_{\max})/(90 - \phi_{\max})] & \phi \geq \phi_{\max} \end{cases}. \quad (2)$$

Our adopted form of the Sromovsky et al. (1993) zonal wind profile is

$$u_s(\phi) = T(u_{\text{Sromovsky}}(\phi), 75°). \quad (3)$$

Since the atmospheric occultations probed the microbar regime,[3] we allowed for a possible variation in the strength of the zonal wind over this large pressure interval. We define $W(p)$ to be a pressure-dependent nondimensional factor by which the nominal zonal wind profile, $u_s(\phi)$, is scaled:

$$U_s(p, \phi) = W(p)u_s(\phi). \quad (4)$$

[3] We find $p_{1/2} = 0.7\ \mu$bar as a typical value for the pressure of the half-light level, many scale heights above the $p_{\text{cloud}} \simeq 100$ mbar level characteristic of the measured clouds.

Thus, $W = 0$ corresponds to a uniformly rotating planet (no winds), $W = 1$ is the full-strength Sromovsky et al. (1993) profile, and intermediate values $0 < W < 1$ represent zonal wind profiles of the same shape but diminished amplitude.

Following the Lindal et al. (1985) prescription, we determined the reference geoid for a uniformly rotating Neptune with a period of 16.11 h (Warwick et al. 1989), assuming physical constants $\text{GM}_N = 6.835107 \times 10^6$ km^3 s^{-2}, $J_2 = 3410 \times 10^{-6}$, $J_4 = -34.7 \times 10^{-6}$, and a reference radius $r_{\text{ref}} = 25225$ km (Owen et al. 1991). It is important to recognize that the reference geoid simply provides a convenient surface with respect to which we calculate *deviations* expected due to nonuniform rotation. In the end, we utilize the true limb shape, which is the sum of the geoid plus the deviations. There is no implicit requirement that the atmosphere actually be in uniform rotation in the Lindal et al. (1985) development, which assumes only that the local perpendicular to a constant potential surface is in the direction of the vector sum of the acceleration associated with the local gravitational field of the planet (expressed in terms of its harmonic coefficients) and the centripetal acceleration associated with the zonal circulation *at that pressure level*. Our analysis is not sensitive to the details of the deep circulation, such as whether or not the atmosphere rotates on cylinders below the cloud deck. The constant potential surface at any given level does not depend on the zonal flow at deeper levels except to the extent that this manifests itself in the zonal harmonics of the gravitational field. (See Hubbard et al. (1997) for a detailed discussion of the shape of the planetary limb in the presence of differential rotation.)

Given an assumed zonal wind with respect to an adopted uniform rotation period, we can calculate the radius of the corresponding potential surface as a function of latitude.

TABLE II
Atmospheric Occultation Measurements

Occ.	Obs.[a]	Ev.[b]	$t_{1/2}$(UTC)[c]	r_{obs}(km)[d]	r_{model}(km)[e]	$\theta(°)$[f]
n1968	DOD	I	15:56:25.5 ± 1.3	24964.1 ± 22.8	24948.4	−39.96
	OKA	I	15:56:55.5 ± 1.2	24940.5 ± 21.0	24942.6	−40.63
	MTS	I	15:56:29.0 ± 2.0	24866.8 ± 31.4	24810.9	−56.04
	DOD	E	16:41:28.0 ± 1.0	25112.5 ± 17.6	25130.2	+13.62
	OKA	E	16:41:51.5 ± 1.0	25130.0 ± 17.5	25132.5	+13.03
	MTS	E	16:36:46.0 ± 2.0	25204.5 ± 31.6	25157.9	−2.29
N30	KAO	I	14:28:15.11 ± 0.30	25166.5 ± 10.0	25156.4	+3.84
	MTS	I	14:27:04.87 ± 1.52	25091.5 ± 35.7	25147.2	−8.56
	AAT	I	14:27:06.62 ± 0.27	25154.5 ± 10.0	25149.6	−7.62
	ANU	I	14:27:06.92 ± 0.57	25148.0 ± 13.3	25149.6	−7.61
	IRTF	I	14:24:51.11 ± 0.29	25149.7 ± 10.0	25157.9	+2.24
	MKO	I	14:24:50.70 ± 0.33	25158.2 ± 10.0	25158.0	+2.23
	KAO	E	14:59:03.48 ± 0.30	24913.7 ± 10.0	24888.0	+46.67
	AAT	E	15:00:27.22 ± 0.27	25004.7 ± 10.0	24985.6	+35.45
	ANU	E	15:00:26.99 ± 1.07	24999.0 ± 25.0	24985.6	+35.45
	IRTF	E	14:56:15.71 ± 0.84	24923.8 ± 18.2	24907.7	+44.43
	MKO	E	14:56:17.84 ± 1.84	24970.2 ± 40.0	24908.1	+44.39
n39	CTIO	I	5:17:31.7 ± 0.2	25083.5 ± 10.0	25065.4	−25.13
	ESO	I	5:17:26.8 ± 0.2	25079.7 ± 10.0	25066.6	−24.96
	IRTF	I	5:28:17.7 ± 0.2	25139.6 ± 10.0	25140.4	−10.82
	CFHT	I	5:28:16.7 ± 0.2	25150.1 ± 10.0	25140.4	−10.83
	WHT	I	5:23:05.0 ± 5.0	25158.4 ± 53.4	25145.6	−9.13
	LOW	I	5:22:18.4 ± 1.2	25132.6 ± 12.8	25145.3	−9.26
	CTIO	E	6:34:59.9 ± 0.2	25101.8 ± 10.0	25095.8	+20.40
	ESO	E	6:34:55.4 ± 0.2	25104.7 ± 10.0	25094.8	+20.56
	IRTF	E	6:41:16.6 ± 0.2	24999.3 ± 10.0	24980.9	+36.00
	CFHT	E	6:41:17.6 ± 0.2	25010.4 ± 10.0	24980.9	+35.99
	WHT	E	6:36:17.0 ± 5.0	24976.2 ± 53.0	24973.5	+36.86
	LOW	E	6:35:43.9 ± 1.2	24986.4 ± 12.7	24975.6	+36.61
N51	OPMT	E	21:10:36.05 ± 2.40	25065.5 ± 10.0	25054.9	+26.59
N55	ESO2	I	23:47:30.2 ± 1.0	25127.3 ± 10.0	25131.0	−13.34
	ESO1	I	23:47:30.2 ± 1.0	25127.4 ± 10.0	25131.0	−13.34
	OPMT	I	23:44:30.6 ± 1.0	25166.1 ± 10.0	25157.7	+2.53
	ESO2	E	00:22:18.7 ± 1.0	25095.4 ± 10.0	25088.0	+21.66
	ESO1	E	00:22:18.7 ± 1.0	25095.2 ± 10.0	25088.0	+21.66
	OPMT	E	00:16:42.7 ± 1.0	24989.0 ± 10.0	24976.2	+36.49

[a] Observatory codes. DOD, Dodaira; OKA, Okayama; MTS, Mt. Stromlo; KAO, Kuiper Airborne Observatory; AAT, Anglo-Australian Telescope; ANU, Siding Spring 2.3 m; IRTF, NASA Infrared Telescope Facility; MKO, University of Hawaii 88''; CTIO, Cerro Tololo Interamerican Observatory; ESO, European Southern Observatory 3.6 m; CFHT, Canada–France–Hawaii Telescope; WHT, William Herschel Telescope; LOW, Lowell Observatory; OPMT, Pic du Midi; ESO2, ESO 2.2 m; ESO1, ESO 1 m.

[b] Atmospheric event: immersion (I) or emersion (E).

[c] Estimated half-light time from isothermal fit to light curve. Errors are formal errors of the fit.

[d] Computed radial distance of occultation point from center of planet. Estimated uncertainty is the larger of 10 km ($\simeq 0.25H$) and the propagated radius error from $t_{1/2}$.

[e] Radius computed from the limb shape model of Table I. Add 104 km to the tabulated values of r_{obs} and r_{model} to correct for general relativistic and refractive bending.

[f] Neptune latitude of sub-occultation point.

For convenience, we represent this as a height deviation from the reference geoid. Representative wind profiles for a range of wind scale factors are shown in Fig. 3, along with the corresponding latitude-dependent height above the reference geoid. The centripetal acceleration associated with the zonal winds produces deviations of tens of kilometers from the approximately elliptical reference ge-

oid. Although the equatorial jet results in an equatorial concavity in the *relative* height with respect to the reference surface, the actual limb curvature is positive everywhere.

We began by fitting the sky plane positions of the half-light times to the appropriately projected model planetary limb for a range of wind scale factors. As shown in the bottom panel of Fig. 8 (Section 4.3), the fits are substan-
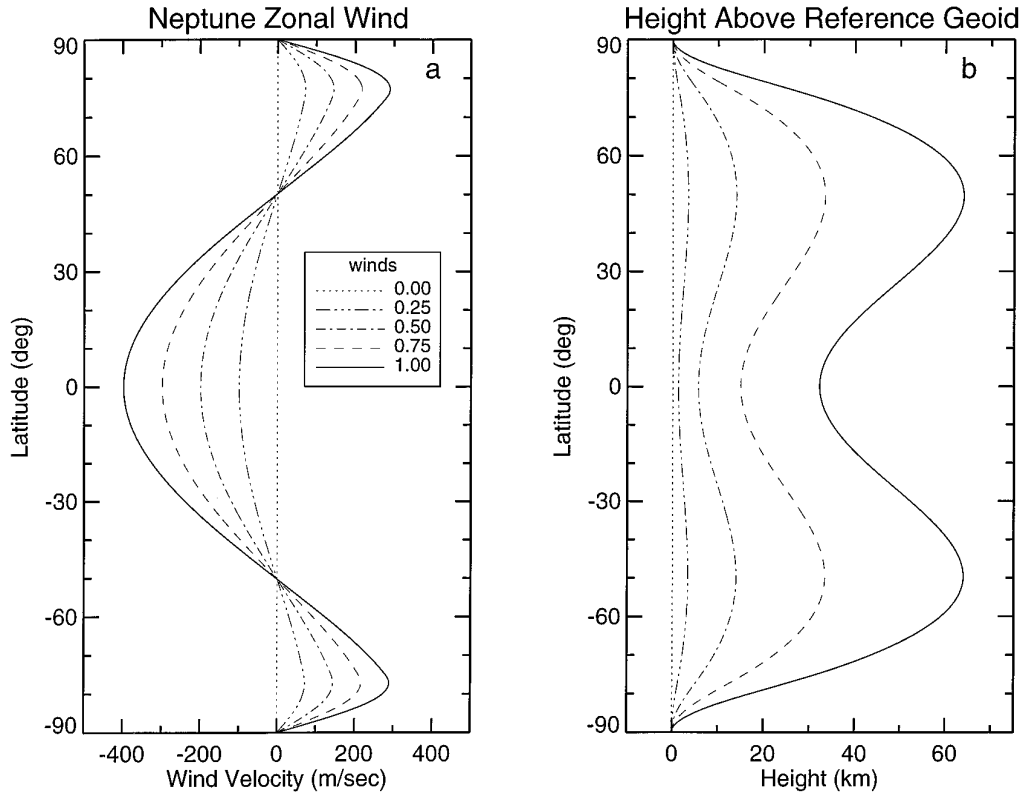
FIG. 3. (a) Zonal wind profile for Neptune based on Voyager cloud measurements (solid) and multiplied by scale factors of $W = 0$, 0.25, 0.5, and 0.75. (b) The effect of the zonal wind profile upon the limb shape for the same profiles shown in (a), where the ''reference geoid'' is the geopotential surface for uniform rotation ($W = 0$).

tially better for W near 0 than for W near 1, with a minimum in χ^2 for $W = 0.17$, indicating that the differential rotation at the half-light pressure level is much weaker than at the cloud deck.[4] Since $W = 0$ corresponds to solid body rotation and a limb shape that is very close to elliptical, we next fitted the limb data to a simple oblate model for a range of ellipticities (see Fig. 13b, Section 5.2). The formal error of the best elliptical fit is comparable to that for the fit with $W = 0.17$, and for simplicity we have adopted the best oblate limb fit as our astrometric solution for the limb data. As shown in Table I, we obtained an equatorial radius at the half-light level of $r_e = (25158.7 + 104) = 25262.7 \pm 3.5$ km and $\varepsilon = 0.0180 \pm 0.0010$ for a fit to the data of Table II.[5]

Representative weighted least squares fits to $r_{1/2}(\phi)$ are shown in Fig. 4 for a range of wind scale factors and for

---

[4] The minimum value of χ^2 is less than one. This may be due to the nonuniform distribution of data in the weighted fit, or it may suggest that the adopted error bars of the fitted data have been overestimated.

[5] The additive factor of 104 km in r_e compensates for the combined effects of atmospheric refractive bending at the half-light level (50 km) and general relativistic deflection of starlight by the planet (54 km).

the best-fitting elliptical limb shape. The uncertainties in the half-light times $\sigma(t_{1/2})$ were transformed to uncertainties in the half-light radius $\sigma(r_{1/2})$ from the center of Neptune. We set a lower limit to $\sigma(r_{1/2})$ of 10 km (approximately 0.25 H, the atmospheric scale height), which experience has shown to provide a more realistic measure of the minimum uncertainty than the formal errors of the isothermal fit.

For the purposes of modeling the central flash observations, the key results from the adopted limb fit are the ephemeris offsets $\{f_0, g_0\}$ for n39, N51, and N55. Note from Table I that there is a relatively small uncertainty in f_0 (just a few kilometers) and a somewhat larger uncertainty in g_0 (a few tens of kilometers). This difference in formal errors is a consequence of the central occultation geometry (Fig. 1): a small error in the length of the chord between atmospheric immersion and emersion results in a relatively large north or south ephemeris correction (g_0). When fitting model lightcurves to the central flash data, we require that the assumed geometry of the central flash be consistent with the constraints supplied by the limb fits.

The N51 event requires special consideration. Only one atmospheric event (emersion) was observed, with a fitted
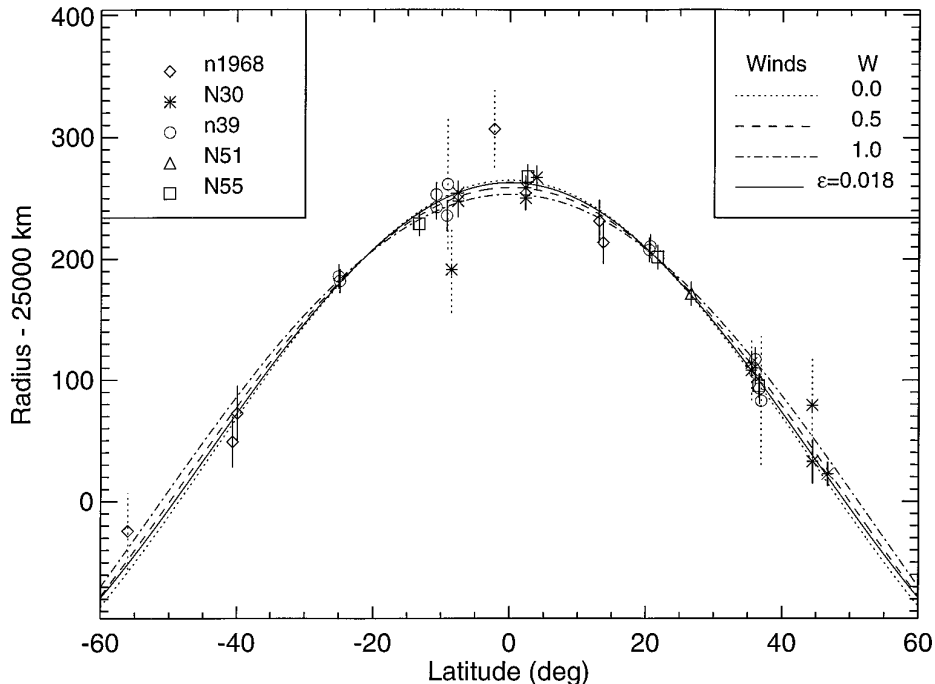
FIG. 4. Fits to the half-light data of five stellar occultations for Neptune limb models with a variety of wind scale factors, W, and for the best-fitting elliptical limb shape with oblateness $\varepsilon = 0.018$. Error bars in excess of ± 25 km are shown dashed to avoid cluttering the figure. The nominal radii of all points have been increased by 104 km to account for general relativistic and refractive bending.

half-light time of 21:10:36.05 UT $\pm$ 2.40 s. From this single measurement, it is not possible to determine both f_0 and g_0 for this occultation. Instead, there is a locus of possible offsets $\{f_0, g_0\}$ such that the planetary limb passes precisely through the emersion $t_{1/2}$ sky plane point. We will return to this point in Section 4.3 when we consider the geometry of the N51 central flash.

4. MODELS OF NEPTUNE'S CENTRAL FLASH

A central flash is produced by refractive focusing of starlight by the curved limb of the occulting planet. When the observer passes in the vicinity of the center of the planet's shadow, the focusing by the limb compensates for the strong defocusing of rays by differential refraction perpendicular to the limb, and a momentary brightening of starlight can be observed. In the simplest case, there are two stellar images when the observer's path is outside of the caustic and four limb images when the observer is within the limb focal pattern. The brightness of the individual images depends on the sky-plane separation of the observer and the image locations compared to the radius of curvature of the projected limb at the locations of the images. Lellouch *et al.* (1986) and Hubbard *et al.* (1987) analyzed the n39 atmosphere and central flash observations under the assumption that Neptune's limb is approximately elliptical, and they determined the oblateness at the central

flash pressure level.[6] Subsequently, Sicardy *et al.* (1991) observed the N51 and N55 occultations and concluded that a simple oblate limb model could not be simultaneously fitted to all three central flashes. Additionally, it was recognized that central flash observations could be a sensitive tool for determining differential rotation of a planetary atmosphere. Hubbard *et al.* (1993) developed an inversion technique to determine Titan's zonal winds from a rich set of central flash observations of the 3 July 1989 occultation of 28 Sgr, and Nicholson *et al.* (1995a) investigated the flickering central flash images of the 28 Sgr occultation by Saturn to study Saturn's stratospheric winds. These developments, along with the improved determination of Neptune's pole provided by Voyager observations, prompted us to search for a model of Neptune's limb shape at the p_{flash} level that could match all three central flash events: n39, N51, and N55.

4.1. Effects of Zonal Winds on Central Flash Optics

If the focal pattern of the projected planetary limb were sampled by a dense set of central flash occultation chords,

---

[6] For Neptune, we find the pressure level sounded by the rays forming the central flash to be $p_{\text{flash}} = 0.38$ mbar, using Eq. (1) of Nicholson *et al.* (1995a), or $\simeq 300$ km below the half-light pressure level $p_{1/2} = 0.7$ μbar for a scale height $H = 47.6$ km.
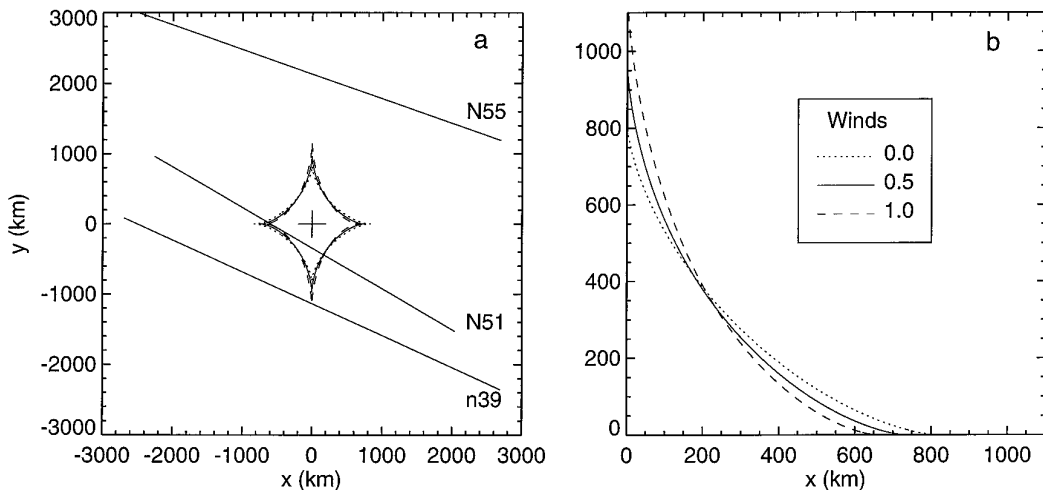
FIG. 5. (a) The focal pattern at Earth of Neptune's limb for wind scale factors of $W = 0$, 0.5, and 1.0, and the occultation tracks for three central flash events. (b) A magnified view of one quadrant of the caustic pattern, showing the effect of differential rotation in Neptune's atmosphere.

the detailed shape of the limb could be recovered by inversion. This is the principle behind the Hubbard *et al.* (1993) technique, but in the present case the three separate central flash observations do not provide enough constraints to determine the limb shape uniquely. Before attempting a full inversion of the observations, therefore, we begin with the more restrictive assumption that at the pressure level probed by the central flash, the latitude-dependent zonal wind profile is proportional to the pattern found by Sromovsky *et al.* (1993) at the $\simeq 100$-mbar level (Eq. (2)). Our search is for the wind scale factor, W, whose corresponding limb shape results in model central flash profiles that best match the observations. In the end, we must assess whether the fit is satisfactory, and if so, to what extent it is unique.

Our prescription for computing model central flash profiles for a specified zonal wind profile is presented in detail by Nicholson *et al.* (1995a) and we will review only the essential features here. The key determinant of the characteristics of a central flash lightcurve is the location of the observer's path across the shadow relative to the caustic pattern of the projected limb. The timing and intensity of the central flash is extremely sensitive to the exact shape of the planet's limb, not primarily because of the slight variations in Neptune's radius, but rather because the slope and curvature of the limb, and hence the locations of perfect focus, are altered. This is illustrated in Fig. 5, where in the left panel we show the apparent paths of each occulted star for n39, N51, and N55 with respect to the planet's center, as projected on the sky. Neptune's caustics are also shown, computed for three different zonal wind models. Here, the y-axis is in the direction of the projected spin axis on the sky and x is the orthogonal sky-plane coordinate. The planetary center is at the origin of this

coordinate system, and the z-axis points toward the observer.[7]

The n39 chord passes just below the southern tip of the caustic, resulting in a sharp flash signal near mid-occultation. As the chord crosses the projected equator, there is a gradual increase in signal as well. The N51 chord intersects the caustic, and when the path lies within the caustic, there are (in the case of an oblate planet) four separate stellar images visible on the limb at locations whose normals intersect the observer's path. The N51 chord also grazes the caustic in the vicinity of the projected equator, making this event particularly sensitive to the limb shape. The two prominent peaks in the N51 central flash lightcurve (Fig. 2) occur when the observer enters and leaves the caustic zone. The more distant N55 chord passes well away from the caustic, and thus both the intensity of the flash and its sensitivity to the exact shape of the limb are diminished.

A magnified view of one quadrant of the caustic is shown in Fig. 5 (right) for wind scale factors of $W = 0$, 0.5, and 1. Note that for the case of uniform rotation ($W = 0$), which is approximately an elliptical limb shape, the polar and equatorial cusps of the caustic are equal in extent— approximately 800 km in this instance. To first order, varying the oblateness of the limb changes the size of the caustic, but not its shape. In contrast, as the wind scale

---

[7] It is sometimes conceptually more helpful to think of the caustic as a fixed focal pattern in space, produced by the star and the planet and to imagine that the orbital and rotational motion of Earth carries the observer through this pattern. In this view, the solid lines in Fig. 5 represent the observer path in the shadow plane at Earth, rather than the apparent stellar path in the sky plane at the planet. Except for minor effects of refraction and general relativistic deflection, the two views are entirely equivalent.

factor is increased, the retrograde equatorial jet has the effect of flattening out the projected limb at the equator (Fig. 3) and moving the tip of the equatorial caustic closer to the center of the planetary shadow. In contrast, the polar cusp of the caustic increases in size along with wind scale factor. Thus, varying the assumed wind strength between $W = 0$ and $W = 1$ will transform the caustic shape between the two extremes shown in Fig. 5. This, in turn, affects the timing and intensity of the model light curves.

As a central flash occultation proceeds, the number, location, and intensity of the separate stellar images on the limb will vary. In the case of the 28 Sgr Saturn occultation (Nicholson *et al.* 1995a), the observations were taken with infrared arrays, and lightcurves for separate individual limb images could be obtained. This would be difficult to achieve for Neptune, given its small angular extent. In any event, the Neptune central flash observations were all made with aperture photometers, and the central flashes correspond to the *combined* intensity of all limb images present at a given time. Figure 6 illustrates the sensitivity of the predicted integrated point source central flash intensity to variations in the wind scale factor. For the n39 occultation, the central spike of the model lightcurve sharpens and intensifies with increasing winds. This is because the tip of the caustic moves closer to the n39 observer path as the wind strength is increased (Fig. 5). The N51 model central flash lightcurves vary substantially near 19:05 UT, corresponding to the location along the track where the observer grazes the caustic. Finally, the N55 model lightcurve shows a slight enhancement near 00:05 UT as the wind scale factor is increased. As for n39, this is because the tip of the polar caustic cusp is closer to the occultation track as the winds are increased, resulting in more effective focusing by the polar limb. However, the N55 flash is much less sensitive to the detailed wind profile than n39 and N51 because the occultation path was well removed from the caustic throughout the event.

4.2. Location of Individual Limb Images

Since the individual images contribute their own signature to the composite observed central flash lightcurve, it is useful to study these images in more detail. The individual model lightcurves for each of the images are shown in Fig. 7 for all three occultations. In the top row, the predicted point source intensity for each image is shown as a function of time, along with the total intensity of the images. The locations in latitude of each of the images are shown as a function of time in the middle row of plots in Fig. 7. The thickness of each line is proportional to the predicted intensity of that particular stellar image. Notice that each of the central flash profiles is sensitive to different latitude ranges on the planet. The n39 event is affected most strongly by the winds at latitudes between 60° and 75°, the N51 event
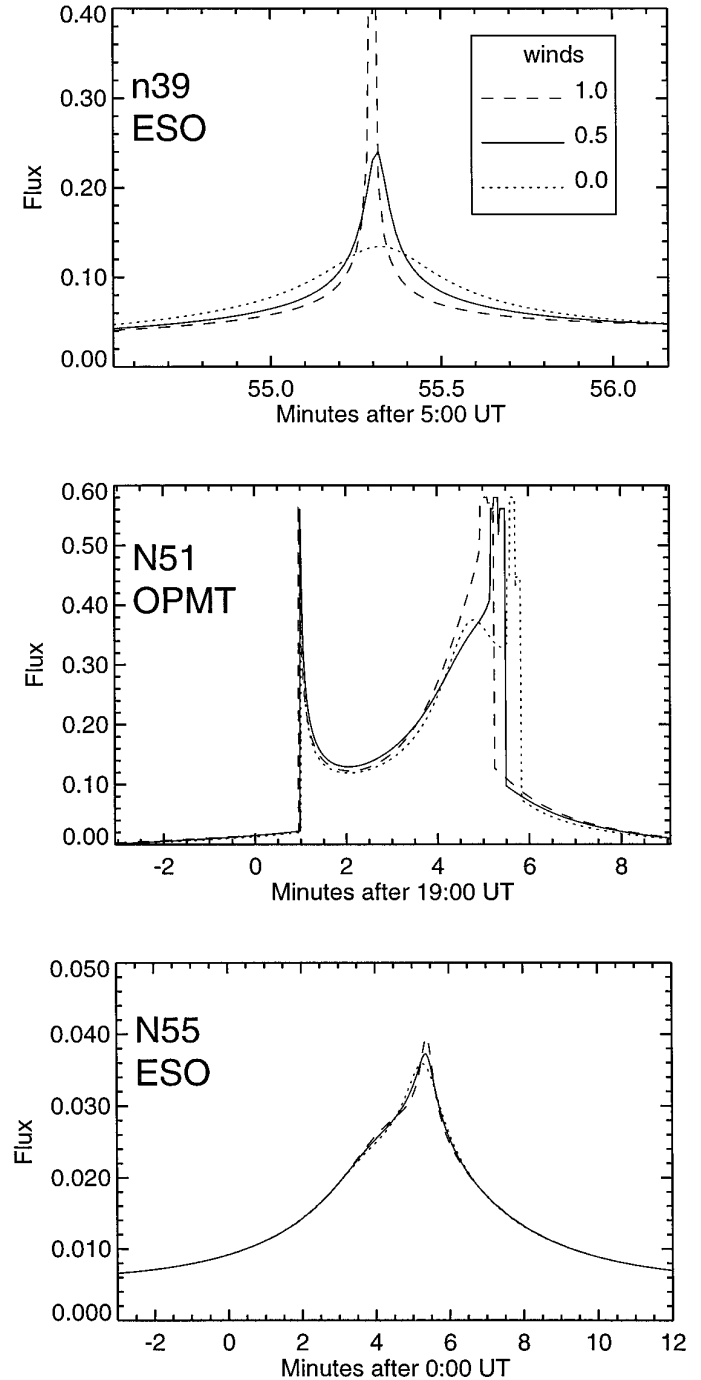
FIG. 6. The sensitivity of the predicted central flash profiles to the strength of Neptune's zonal winds.

to latitudes between 35° and 65° and between 0° and −30°, and the N55 central flash to latitudes between −50° and −65°. The bottom row of Fig. 7 shows the orientation of Neptune, its caustic (to scale), the observer path, and the location of the individual images for the times marked by the vertical dashed lines in the top two rows of the figure.
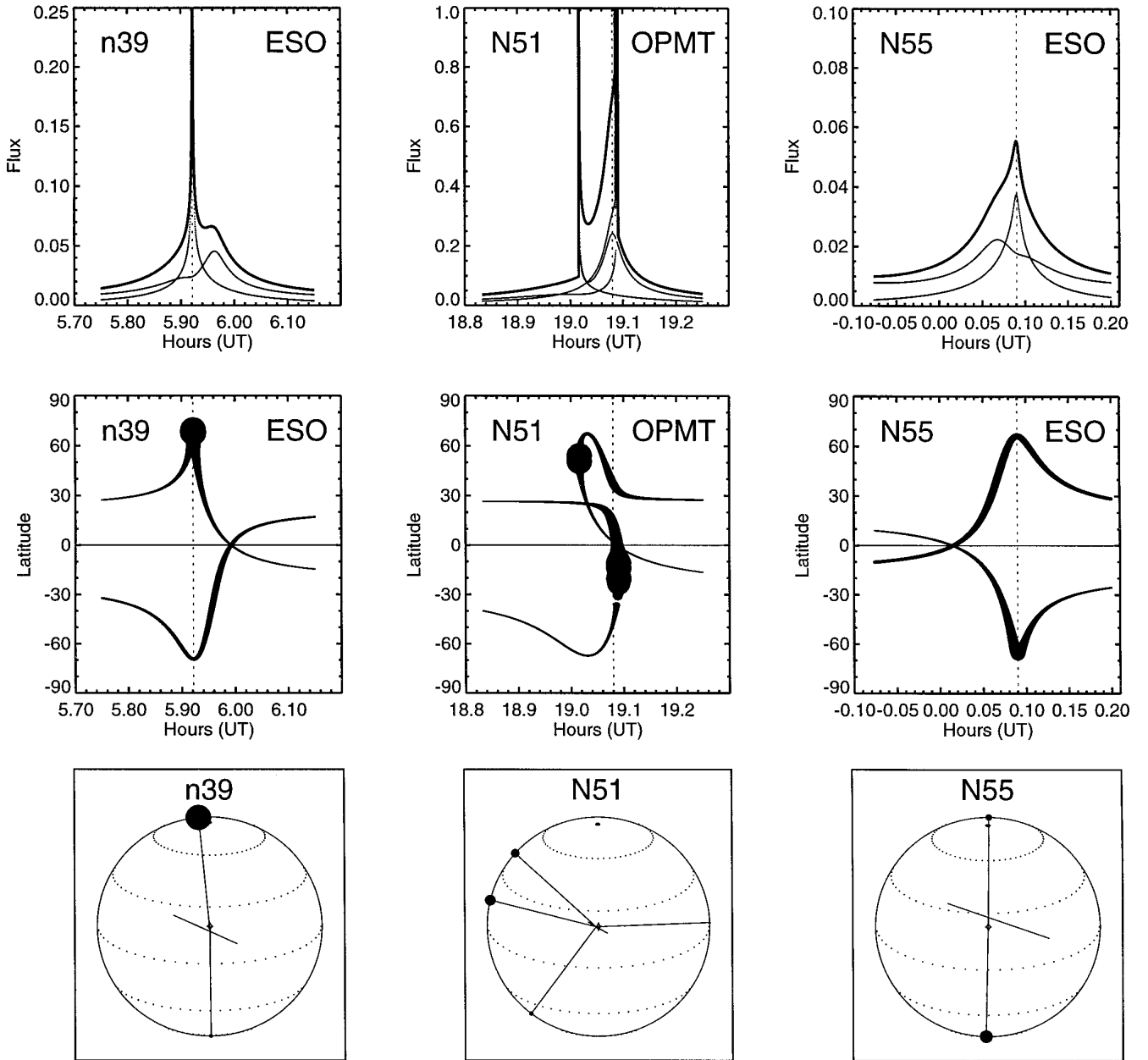
FIG. 7. (Top row) Model central flash profiles for n39, N51, and N55, showing both the light-curves for each individual flash image and the combined flux from all limb images (the thick-lined top curve in each plot). (Middle row) The latitude of the locations of the limb images, plotted as a function of time. The thickness of the line is proportional to the intensity of each image. (Bottom row) Earth views of Neptune, showing the locations of the limb images for each central flash for the times marked by the vertical dashed line in the middle row of plots. The observer's path in the shadow plane and the caustic are shown to scale at the center of each plot, and the sizes of the filled circles are proportional to the intensity of each limb image.

The size of the black dot at the image location is proportional to the predicted intensity of the signal.

From Fig. 7, we see that there are only two images present for the entire n39 central flash. This is because the observer path always lies outside of the caustic (Fig. 5). The strong spike at 5.92 UT comes from an image at high

northern latitudes while the broad shoulder in the lightcurve at 5.97 UT comes from the image at mid-southern latitudes. The situation for N51 is more complex. Prior to crossing the caustic at about 19.02 UT, there are two faint mid-latitude images, but upon entering the caustic another image appears on the northwest limb at about

+55° latitude. This bright image is responsible for the first bright peak in the observed N51 central flash. It rapidly separates into two distinct images, one moving across the northern limb of the planet toward the east and the other moving toward the western equator. Subsequently, the initial pair of faint mid-latitude images brighten, converge, and eventually merge at about 19.09 UT, as the observer leaves the caustic. Thus, the broader feature associated with the second spike in the N51 central flash comes from several images at once, but primarily from the two coalescing southern hemisphere images just prior to their annihilation.

Since the N55 chord is so far removed from the caustic, only two images are present throughout the central flash. Although their *combined* effect results in a smooth intensity feature in the lightcurve, their individual contributions are quite different. In particular, the high southern latitude image produces a rather sharp, narrow intensity spike at about 0.09 UT. As the wind scale factor is increased, this feature becomes much more prominent.

4.3. Least Squares Fits to the Central Flash Lightcurves

Having established the qualitative characteristics of each of the three central flash events, we next describe the procedure we used to fit the observations. We began with the astrometric solution provided by the adopted fit to the atmospheric half-light points. This provided an initial set of planet offsets f_0, g_0 to use for modeling the central flash lightcurves. For n39 and N51 the formal uncertainties in f_0 are $\sigma(f_0) \sim 4$–5 km, whereas $\sigma(g_0) \sim 21$ km. This tighter constraint on the east–west position of the planet compared to the north–south position is a direct consequence of the central flash occultation geometry (Fig. 5). When modeling the central flash observations we give ourselves the freedom to allow the assumed planet offsets to differ from the nominal values, but not by more than the uncertainties given in Table I. For each central flash event, we thus have a pair of df_0 and dg_0, which represent differential planet offsets to be added to the nominal f_0 and g_0 values. For the N51 event, we constrained df_0 and dg_0 to the set of possible values for which the atmosphere emersion point fell exactly on the fitted limb.

We fitted the lightcurves by weighted least squares as follows. For a given wind scale factor W, we first computed the corresponding limb shape at the pressure level probed by the central flash, projected appropriately for each occultation. The predicted central flash intensity was computed by first finding the points on the projected limb whose normals passed through each point along the central flash observer path and then determining the intensity F of each limb image

$$F \simeq \frac{r_c H}{r |d|}, \qquad (5)$$

where r_c is the local radius of curvature of the projected limb at the location of the limb image, $H = 47.6$ km is the scale height of the model isothermal atmosphere, r is the distance in the shadow plane of the observer from the limb image, and d is the distance in the shadow plane of the observer from the point of perfect focus. Geometrically, the factor of H/r in Eq. (5) corresponds to the refractive defocusing of the exponential atmosphere, and $r_c/|d|$ represents the focusing due to limb curvature (see Nicholson *et al.* (1995a) for additional details). The data sets were normalized by the full stellar intensity, and were weighted in the fit by the inverse of the variance in the signal determined in a quiescent region away from the central flash. Our model prediction for the observed central flash profile for a single event is thus

$$I_{\text{model}} = dI + e^{-\tau} \sum_{i=1}^{n} F_i, \qquad (6)$$

where we have summed the flux of the individual flash images, attenuated by $e^{-\tau}$, and offset in normalized intensity by dI.

In practice, the dI is quite small and simply represents a slight correction to the nominal zero level during the central flash. The exponential factor $e^{-\tau}$ is included to accommodate the observation that all three central flashes are weaker than predicted by a model of a transparent, isothermal atmosphere. Lellouch *et al.* (1986) regarded the attenuated signal as evidence of absorption by methane. Alternatively, Hubbard *et al.* (1987) proposed that the observed reduction in central flash intensity is due to a decrease in temperature from 150 to 135 K as the pressure rises from 1 to 400 μbar. In principle, it might be possible to discriminate between these two alternatives because of the different strengths of the CH_4 absorption bands at the multiple wavelengths of our observations, but we will not explore this issue here.

A final complication concerns the smoothness of the observed central flash profiles compared to the abruptness of the predicted lightcurves as the caustic is crossed. Similar smoothing was evident in the first observed central flash, the 1976 Mars occultation of ε Gem (Elliot *et al.* 1977), and is also evident in the N51 lightcurve (Fig. 2). In the 28 Sgr Saturn central flash, Nicholson *et al.* (1995a) also found that the model lightcurves had to be smoothed to provide the best match to the data. The required degree of smoothing (several tens of kilometers) is much greater than that required simply by the projected size of the occulted stars at Neptune (a few kilometers). It seems more likely that it arises from turbulence or other small-scale irregularities in the atmospheric structure. Hubbard *et al.* (1988) and Narayan and Hubbard (1988) discuss anisotropic scintillation in Neptune's occultation shadow in the

context of the n39 occultation. The degree of smoothing required to match the observations may ultimately provide a novel and illuminating constraint on the nature of turbulence. However, we have simply allowed s, the width of the boxcar smoothing function, to be a free parameter in the fit.

In its most general form, our least-squares fitting algorithm included the following free parameters for each central flash profile: sky plane offsets to the nominal atmospheric limb fit (df_0 and dg_0), the normalization parameters dI and $e^{-\tau}$, and the smoothing factor s. We also allowed the parameters of the assumed zonal wind profile to be fitted. In the case of the scaled Voyager wind profile, we fitted for the wind scale factor, W, although we will describe other choices later on. The fitting algorithm was designed to allow the full set of model parameters to be fitted simultaneously, but we found early on that the χ^2 hypersurface was not smooth, and that standard gradient minimization methods would find local but not global minima. Part of the reason for this can be understood by looking at the geometry of the N51 flash (Fig. 5). Note that it requires only a small displacement of the occultation chord south or east to cause the observer path to cross to the outside of the caustic and back inside again, instead of grazing the caustic from inside. As soon as the observer is outside of the focal pattern, two bright limb images disappear, resulting in a discontinuous change in the total flash brightness. Such discontinuous flux changes are evident in Fig. 6 (middle) for N51, near 19:05 UT. After experimenting with simplex methods, we ultimately settled on a time-consuming but thorough search over a wide range of plausible parameter values.

We fitted each lightcurve separately, over a range of W between -0.5 and 1.5. Each of the central flash events required special treatment. For n39, we found that there was a strong correlation between W and dg_0. Geometrically, this is because the north–south extent of the caustic changes with W (Fig. 5), and moving the observer chord south or north by dg_0 mimics the effect of changing the wind speed. Fortunately, the limb fit to the half-light data gave a fairly tight constraint on g_0, and by requiring that $|dg_0| < \sigma(g_0)$, this behavior was avoided. In the end, we simply forced $dg_0 = 0$ and allowed df_0 to be a free parameter to allow for a small along-track position shift of the model curve. The best fitting df_0 was only 5.5 km, very close to the formal uncertainty in f_0 for n39. The results of this series of fits are shown in Fig. 8 (top), where we have plotted as a dashed line the χ^2 of the series of fits as a function of W, the wind scale factor. The fit is best for $W \simeq 0.5$, and is considerably worse for W near 0 or $W > 1$. Changing g_0 by ±21 km (1σ) changed the best fitting W by only ±0.05.

Model experiments for the N51 event quickly showed that the predicted lightcurve varied drastically with slight
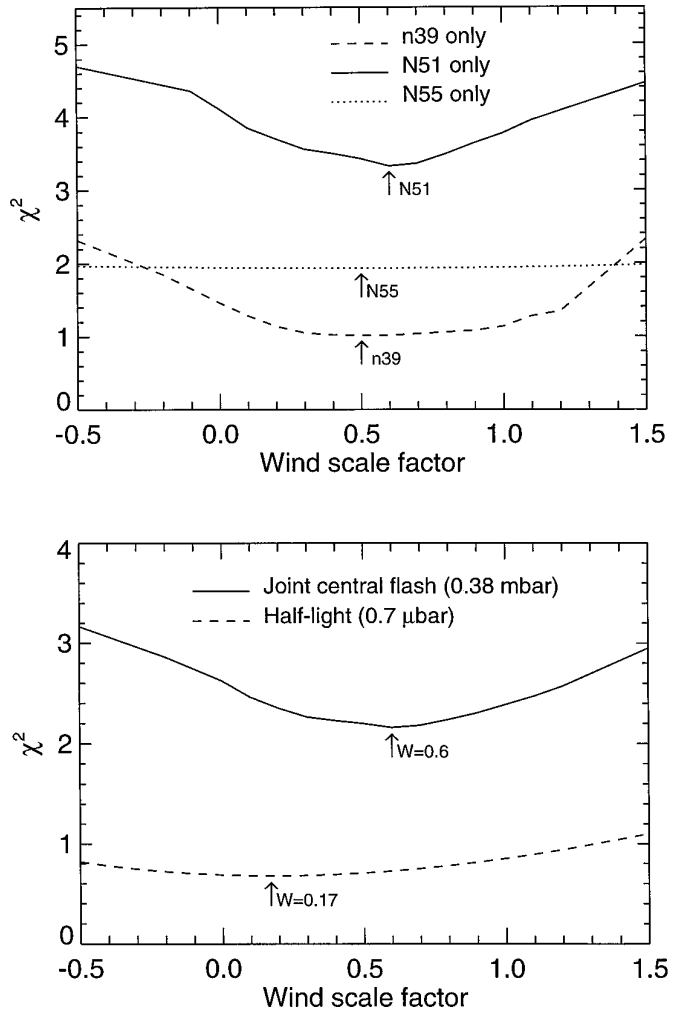
FIG. 8. (Top) Results of least-squares fits to the individual central flash lightcurves. For each central flash event, the wind scale factor W was varied between -0.5 and 1.5, and for each value of W, the parameters df_0, dg_0, dI, $e^{-\tau}$, and s were varied to give the best fit to the observations. Here, χ^2 is plotted as a function of W. For all three occultations, the best fits are for intermediate wind scale factors, as marked by the vertical arrows. The n39 and N51 occultations constrain W quite strongly. (Bottom) The solid line shows χ^2 for a series of joint fits to the n39, N51, and N55 central flash light curves as a function of W. The best fit is for $W \simeq 0.6$, marked by an arrow, with substantially worse fits for W near 0 or 1. The dashed line shows the results of a series of fits to the half-light atmosphere data, probing a pressure level of $p_{1/2} = 0.7$ μbar, as a function of wind scale factor. The best fit is for $W = 0.17$, indicating that there is less differential rotation at these higher levels than in the deeper central flash region, which sounds a pressure level of $p_{\text{flash}} = 0.38$ mbar.

changes in f_0 and g_0. Even though the f_0 and g_0 were not uniquely determined from the half-light limb fit, the central flash profile gave an exceedingly tight constraint. For each W, we restricted the possible values of df_0 and dg_0 for N51 to lie on a curve such that the single emersion half-light point was exactly on the limb of the planet, and we computed a dense set of models along this df_0, dg_0 line. For

TABLE III
Central Flash Fit Results

Parameter	n39	N51	N55
df_0(km)	5.5 ± 1.4	(-4)	(0)
dg_0(km)	(0)	(18)	(0)
dI	-0.0082 ± 0.0003	-0.0363 ± 0.0033	-0.0007 ± 0.0003
$e^{-\tau}$	0.809 ± 0.006	0.593 ± 0.003	0.69 ± 0.01
τ	(0.21)	(0.52)	(0.37)
Smoothing (km)	(28)	(31)	(33)
	Wind scale factor $W = 0.6 \pm 0.2$		

each W, df_0, dg_0 trio, we determined by least squares the best-fitting values of dI, $e^{-\tau}$, and s, and then selected the df_0, dg_0 pair that gave the best fit for this W. The solid line in the top panel of Fig. 8 shows the variation of χ^2 with W. Once again, there is a distinct minimum at moderate wind scale factors, with the best fit at $W = 0.6$ and substantially worse fits near $W = 0$ and 1. In our fits, we assumed the same attenuation factor $e^{-\tau}$ for each of the separate images that produced the integrated central flash signal. It is possible that different attenuation factors are appropriate for the northern mid-latitude images that produced the first peak in the central flash and the southern low-latitude images that produced the second peak (see Fig. 7). However, we find from numerical experiments for this event that the derived wind scale factor is sensitive primarily to the absolute timing and width of the central flash peaks, not to the amplitude of the flash. (The correlation coefficient between W and $e^{-\tau}$ is only 0.3.)

The N55 central flash chord is so far from the caustic that it changes only very slightly with df_0 and dg_0. For this event, we set df_0 and dg_0 to zero, fixed the smoothing at a value comparable to that for n39 and N51, and fitted only for dI and $e^{-\tau}$ for each value of W. The dotted line in Fig. 8 (top) shows the very weak dependence of χ^2 on the assumed wind speed for this event, although there is a minimum in the χ^2 curve near $W = 0.5$.

Once we had found the best separate solutions for the individual central flashes, we repeated the process with a sequence of simultaneous fits to all three data sets (weighted as previously described), over the same range of wind scale factors as before. Table III shows the results of our adopted joint fit. The χ^2 curve for these joint central flash fits is plotted as a solid line in the bottom of Fig. 8. The best fit has a wind scale factor of $W = 0.6 \pm 0.2$, where the error estimate takes into account possible systematic errors in the assumed planet center positions df_0 and dg_0, variations in the best fitting W for each occultation, and the sensitivity of the joint fit to W.

The models match all of the observations remarkably well. Figure 9 shows each of the flashes, the model lightcurve from our adopted solution, and the residuals of the fit plotted below each flash profile. To illustrate the

sensitivity of our fits to different values of W, we have plotted the differences between the $W = 0.6$ solution and two other models: $W = 0.3$ and $W = 0.9$. The top left panel shows the global fit to the n39 central flash complex. The feature near 6:00 UT was excluded from the fits; it is probably due to scintillation (see Hubbard *et al.* 1988) and cannot be matched by any of our smooth limb models. However, the sharp central spike (shown at an expanded scale in the top right panel), the broad shoulder, and the overall shape of the central flash are nicely reproduced by the model. Our fitted value of $e^{-\tau} = 0.809$ is in excellent agreement with the Lellouch *et al.* (1986) result of $0.82^{+0.21}_{-0.16}$ (modified to take into account the difference between our assumed atmospheric scale heights).

The bottom left panel shows the asymmetrical N51 central flash and the best fitting model. Note that the asymmetric shape and the ramped edges as the caustic is crossed are matched by the model. The systematic variations in the residuals near 18:55 UT and 19:07 UT are well-removed from the central flash region itself. Finally, the low-amplitude N55 flash is nicely fitted by our adopted limb model, as shown in the bottom right panel.

4.4. Direct Retrieval of the Zonal Wind Profile

In our analysis, we have assumed that the latitudinal variation of the zonal wind at high altitudes resembles that just above the clouds. The excellent fits to the central flash data are consistent with this supposition, but the available observations do not exclude other possibilities, since the central flashes are not equally sensitive to wind speeds at all latitudes. As we pointed out above, in principle it is possible to retrieve Neptune's zonal wind profile at the p_{flash} level directly from the central flash observations themselves, without resorting to scaling of Voyager cloud motion measurements from the much deeper p_{cloud} level. If the general shape of the wind profiles were quite different at these two levels, then the simple one-parameter model of Eq. (4) would be inappropriate and possibly misleading as well.

To explore this possibility, we adopted two generalized representations of the zonal wind profile. In the first, we expressed the wind profile as a series of low-order Legendre polynomials:

$$u_{\text{Legendre}}(\phi) = \sum_{i=0}^{n} c_i P_i(\sin \phi). \tag{7}$$

As before, we applied a cosine taper to prevent infinite wind speeds at the poles:

$$u_l(\phi) = T(u_{\text{Legendre}}(\phi), 75°). \tag{8}$$

The coefficients c_i are the parameters to be determined by
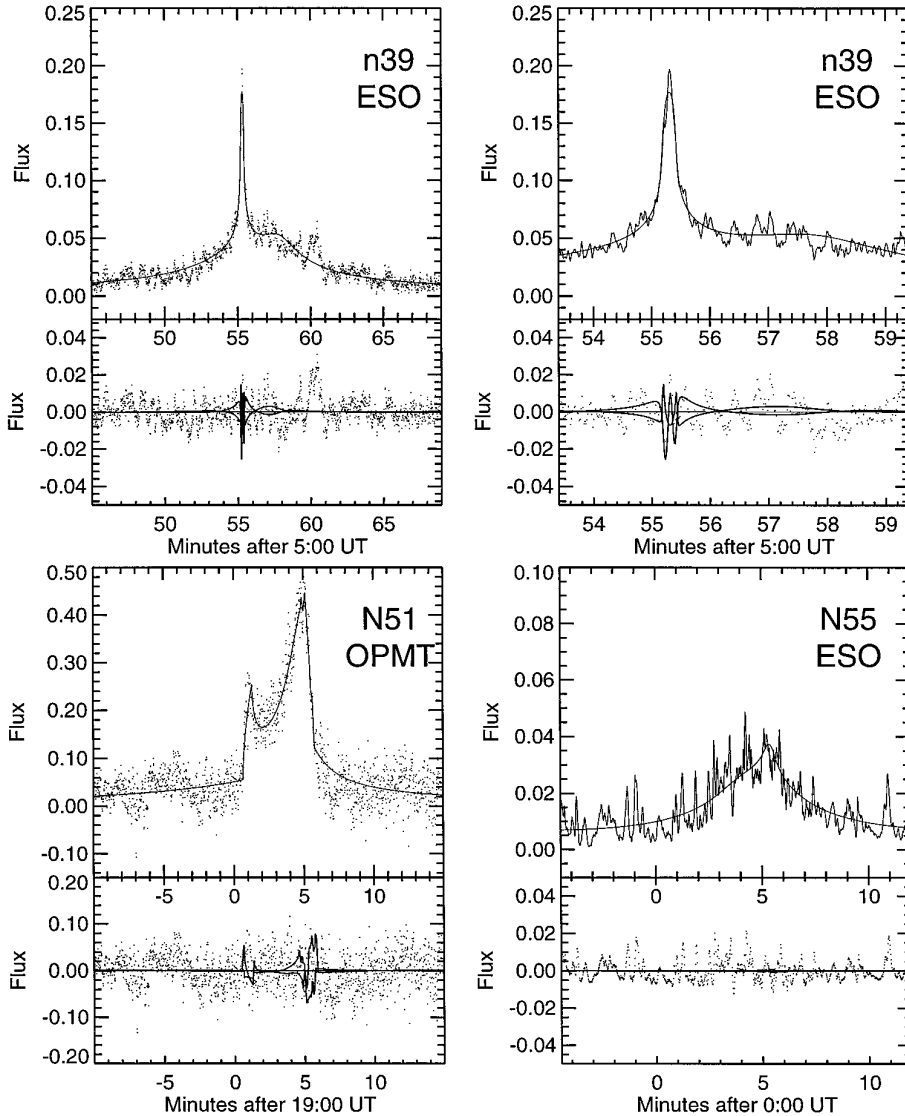
FIG. 9. Comparison of the central flash observations for each occultation with model lightcurves computed from our adopted fit (Table III) and residuals. The differences between models with $W = 0.3$ and those with $W = 0.9$ and the adopted fit value of $W = 0.6$ are overplotted on the residuals to illustrate the sensitivity to W of each lightcurve.

optimizing the match between the central flash models and the observations. Even values of i correspond to basis functions which are symmetric about the equator. As an alternative basis set, we used Fourier series

$$u_{\text{Fourier}}(\phi) = b_0 + \sum_{i=1}^{n} [a_i \sin(2i\phi/360) + b_i \cos(2i\phi/360)],$$

$$(9)$$

which, in its tapered form, is

$$u_{\text{f}}(\phi) = T(u_{\text{Fourier}}(\phi), 75°). \qquad (10)$$

In this case, the cosine terms are symmetric about the equator.

Whereas for the analytical wind profile of Eq. (4) we had only one free parameter, the wind scale factor W, in the case of the Legendre or Fourier series the parameter space of the unknown coefficients is potentially quite large. Since we used an inefficient but thorough search method to avoid settling into a false local minimum in χ^2-space, we restricted our attention to low-order expansions that were symmetric about the equator in order to keep the computation time within reasonable limits. In Fig. 10, we show the results of our retrievals. Quantitatively, the Fourier and Legendre fits had figures of merit essentially identical to the best fit using the scaled Voyager results. Our adopted best-fitting scaled Voyager profile, used for the models in Fig. 9, is shown as a solid line. The best Legendre polynomial retrieval is shown as a dashed
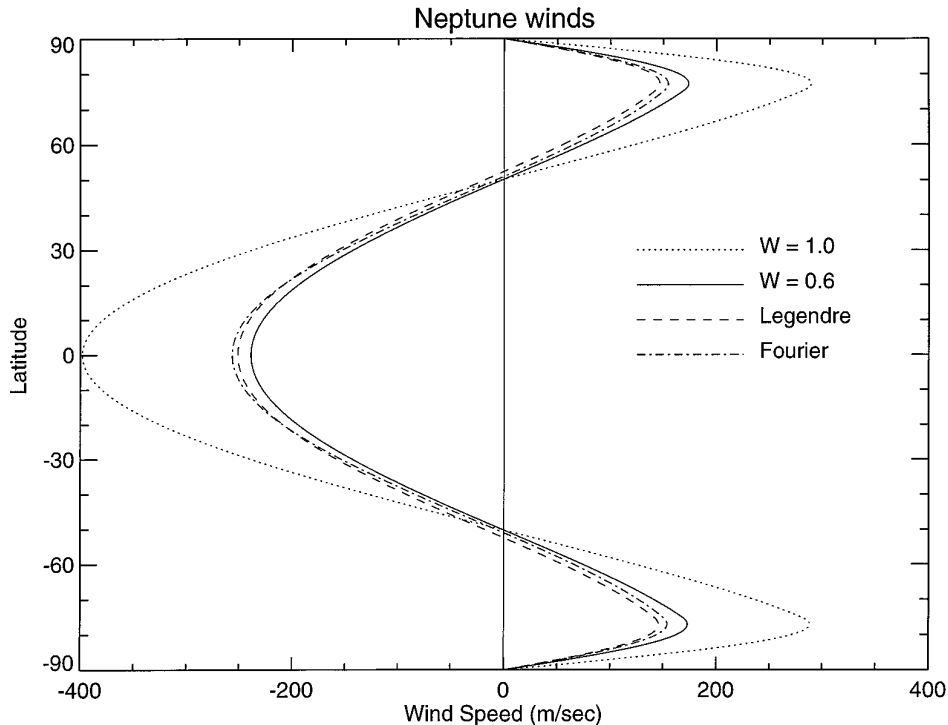
FIG. 10. Neptune zonal wind profiles at the p_{flash} = 0.38-mbar level, obtained from direct retrieval and joint model fits to the n39, N51, and N55 central flash observations. All wind profiles have been tapered to zero velocity at the poles. The observed Voyager wind profile at p_{cloud} = 100 mbar is shown as a dotted line, corresponding to a wind scale factor of $W = 1$. In contrast, the winds at the central flash level have diminished substantially. The best-fitting scaled Voyager wind profile ($W = 0.6$) is shown as a solid line. Also shown are the results of two low-order retrievals of the wind profile obtained without assuming that the central flash winds have the same shape as the Voyager profile. We represented the zonal wind profile as a sum of the first three even Legendre polynomials, and as the first three cosine terms in a Fourier series, and determined the corresponding coefficients that gave the best match to the observations. All three of the resulting central flash wind profiles are very similar, suggesting that the Voyager wind profile is a reasonable representation of latitude-dependence of the zonal flow at the pressure levels sounded by the central flash.

curve, where c_0, c_2, and c_4 were fitted and all other coefficients were set to zero. The best Fourier series retrieval is shown as well, with nonzero coefficients b_0, b_1, and b_2. For comparison, the cloud-level Voyager wind profile is shown as a dotted line. The three wind profiles fitted to the central flash observations are all very similar, showing an equatorial retrograde jet and weaker prograde flow at mid- to high latitudes. One should probably not make too much of the excellent agreement among the profiles, since we limited our investigation to very low-order expansions. Nevertheless, the comforting lesson from this exercise is that the general character of the winds as obtained from the central flash fits does indeed resemble the Voyager observations, which were fitted by Sromovsky et al. (1993) to polynomials of even powers of the latitude, ϕ, and not to an orthogonal set of basis functions.

5. NEPTUNE'S STRATOSPHERIC WINDS

The results of our model fits to the central flash observations show that Neptune's upper atmospheric winds have decayed in strength from the cloud-top winds. We will use

these results to determine the vertical shear in the zonal wind and to compare the rotation figure of Neptune in the upper stratosphere to that at deeper levels.

5.1. Vertical Shear in Neptune's Zonal Wind

The mean zonal flow determined from cloud motion studies is at much deeper levels than the p_{flash} = 0.38-mbar level of the central flash measurements and the $p_{1/2}$ = 0.7-μbar level of the atmospheric occultations. We can take advantage of these large pressure differences to estimate the vertical shear of the zonal wind between the p_{cloud} = 100-mbar level and the upper stratosphere. As a point of departure, we begin with the Voyager IRIS measurements of the zonally averaged latitude dependence of the temperature between 30 and 120 mbar, obtained from spectra over the range between 200 and 400 cm^{-1} (Conrath et al. 1989). More recent analysis of the IRIS measurements has resulted in improved temperature retrievals, but the general character of the unpublished results is consistent with the Voyager IRIS team's initial
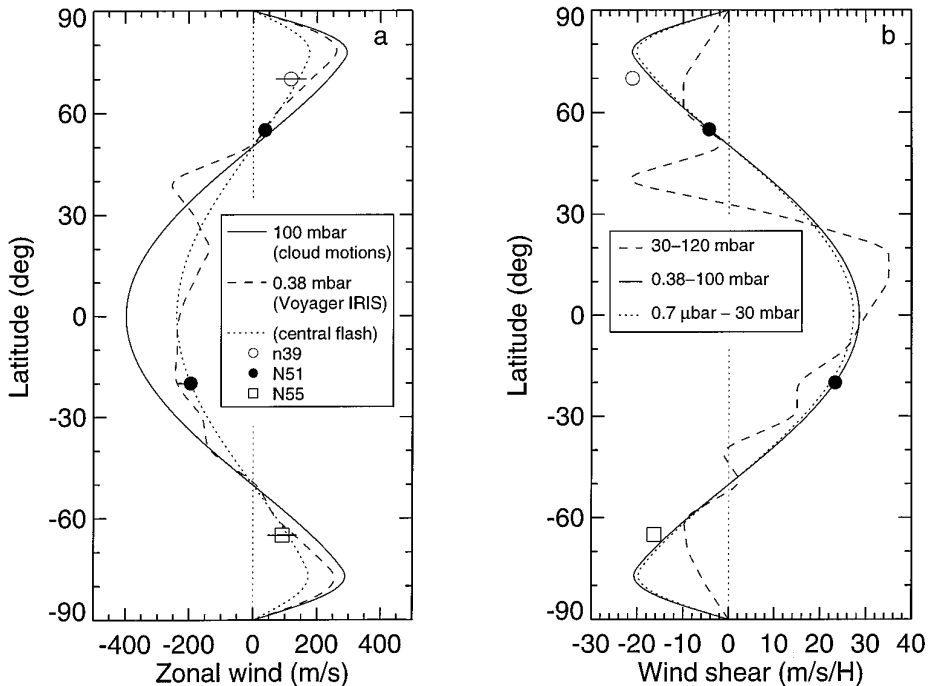
FIG. 11. (a) Neptune zonal winds. The solid line shows the observed $W = 1$ wind profile at the $p_{cloud} = 100$-mbar level from Voyager cloud motion studies. When this wind profile is extrapolated to the $p_{flash} = 0.38$-mbar level, assuming that the Voyager IRIS measurements of the vertical shear between the 30- and the 120-mbar levels are applicable over this entire pressure range, the implied wind profile is as shown by the dashed line. The best overall fit from our central flash fits corresponds to $W = 0.6$ and is shown as a dotted line. The inferred winds at the latitudes probed by the individual central flash profiles are shown as symbols, along with their error bars. They lie very close to the extrapolated Voyager profile, suggesting that winds decay with height between the 30- and 0.38-mbar pressure levels at the same rate as at the deeper levels probed by the Voyager IRIS measurements. (b) Vertical shear in Neptune's zonal winds. The dashed line shows the shear profile obtained by the Voyager IRIS team over the 30- to 120-mbar pressure level, interpolated over the equator and extrapolated to zero at the poles. The solid line shows the inferred mean vertical shear over the interval between $p_{cloud} = 100$ mbar and $p_{flash} = 0.38$ mbar, under the assumption that $W = 1$ for the p_{cloud} wind profile and $W = 0.6$ for p_{flash} winds. The dotted line shows the inferred mean vertical shear between the p_{flash} and $p_{1/2}$ levels, assuming wind scale factors of $W = 0.6$ and $W = 0.17$ at these two levels, respectively. The symbols show the shear determined from our fits to the central flash light curves, at the latitudes probed by these observations.

findings (P. Gierasch and E. Ustinov, pers. commun.). Conrath *et al.* (1989) used the thermal wind equation and the measured meridional gradient along isobars to estimate the latitude-dependence of the vertical shear in the prevailing zonal wind. We have used their wind shear profile (Fig. 7 of Conrath *et al.* 1989), interpolated across the equator and extrapolated to zero at the poles, along with our assumed zonal wind profile at the $p_{cloud} = 100$-mbar level, to predict the zonal wind profile at the $p_{flash} = 0.38$-mbar central flash level. Figure 11a shows the 100-mbar zonal wind profile (solid line) and the corresponding winds (dashed line) at 0.38 mbar under the assumption that the 30- to 120-mbar IRIS shear measurements can be extended all the way up to the central flash pressure level. Also shown is the $W = 0.6$ wind profile (dotted line) found from our best joint fit to the central flash observations. In Fig. 11b the IRIS shear measurements are plotted as a dashed line.

From our central flash fits, we found that a wind scale

factor of $W = 0.6$ gave the best match to the data. The pressure interval from 100 to 0.38 mbar corresponds to $5.57\,H$, and we can estimate the resulting mean vertical shear profile over this interval as

$$\frac{du(\phi)}{dz}\bigg|_{0.38-100\,mbar} = \frac{u_{0.38}(\phi) - u_{100}(\phi)}{\log(p_{cloud}/p_{flash})H}$$
$$= -0.072u_{100}(\phi)/H \quad (11)$$

for $u_{0.38}(\phi) = Wu_{100}(\phi) = 0.6u_{100}(\phi)$. This is plotted as a solid line in Fig. 11b. Similarly, we can compute the mean shear over the $6.3H$ interval between p_{flash} and $p_{1/2}$,

$$\frac{du(\phi)}{dz}\bigg|_{0.7\,\mu bar-0.38\,mbar} = \frac{u_{0.7\,\mu bar}(\phi) - u_{0.38}(\phi)}{\log(p_{flash}/p_{1/2})H}$$
$$= \frac{-0.068u_{100}(\phi)}{H}, \quad (12)$$
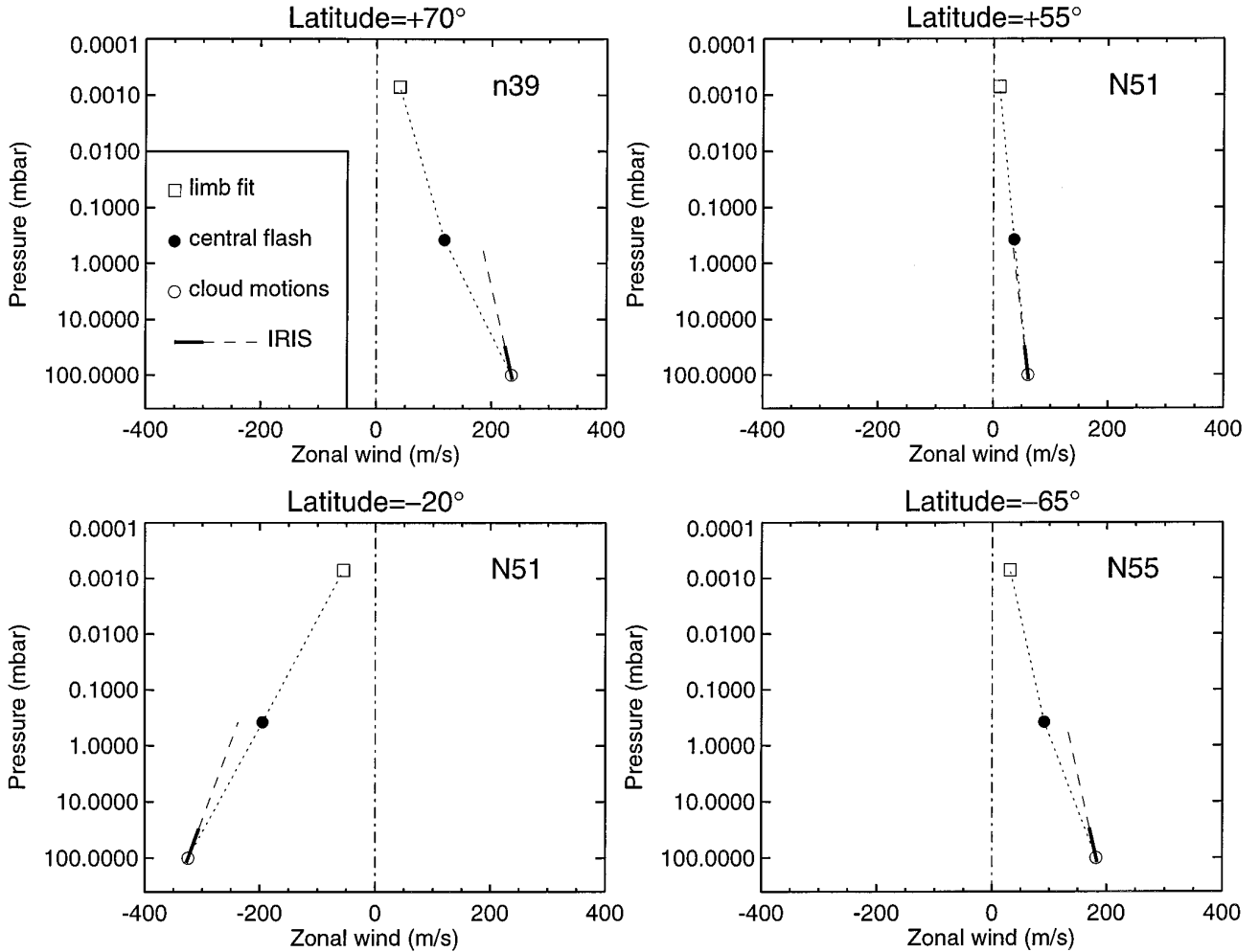
FIG. 12. Zonal winds as a function of pressure at the latitudes probed by the n39, N51, and N55 central flash observations. The winds at the $p_{\mathrm{cloud}} = 100$-mbar level are shown as open circles. The vertical shear between $p = 30$ and $p = 120$ mbar found from Voyager IRIS measurements is shown as a bold solid line, which is extrapolated to the $p_{\mathrm{flash}} = 0.38$-mbar level as a dashed line. The filled circles show the inferred wind speeds from the individual best fits to the wind scale factors for each occultation, and the open squares mark the expected winds at $p_{1/2} = 0.7$ μbar for $W = 0.17$.

for $u_{0.7\ \mu b}(\phi) = W u_{100}(\phi) = 0.17 u_{100}(\phi)$. This is plotted as a dotted line in Fig. 11b. Since each of the individual central flash events is primarily sensitive to a narrow latitude range (Fig. 7), we have plotted separately the inferred mean shear between the 100- and 0.38-mbar levels for each occultation, using the separate best-fitting wind scale factors for each event as shown in Fig. 8a: $W(\mathrm{n39}) = 0.5$, $W(\mathrm{N51}) = 0.6$, and $W(\mathrm{N55}) = 0.5$. The corresponding zonal winds and vertical shears are plotted as symbols in Figs. 11a and 11b.

To illustrate more directly the variation of winds with pressure, we have plotted the derived zonal winds at the latitude of each flash (Fig. 12). The winds at the $p_{\mathrm{cloud}} = 100$-mbar level are shown as open circles for $\phi = 70°$ (n39), $\phi = 55°$ (N51), $\phi = -20°$ (N51), and $\phi = -65°$ (N55). The vertical decay of the zonal winds found from the IRIS

analysis is shown as a bold solid line over the range 30–120 mbar. The dashed line extrapolates this gradient to the central flash level ($p_{\mathrm{flash}} = 0.38$ mbar). The filled circles show the inferred wind speeds from the individual best fits to the wind scale factors for each central flash occultation, and the open squares mark the expected winds at $p_{1/2} = 0.7$ μbar for $W = 0.17$. In all cases, the decay of the winds with height is remarkably constant over the $\sim 12H$ interval between 50 and 75 km above the global cloud deck all the way up to the sub-microbar level in the stratosphere.

Ingersoll (1990) discusses the vertical wind shear below the cloud tops, and points out that the lack of strong latitudinal temperature gradients below the cloud deck implies that the winds are deep. That is, the vertical shear is relatively weak in this region. The thermal structure of the

atmospheres of the four giant planets above the clouds has been determined from Voyager IRIS data (e.g., Conrath and Pirraglia 1983, Gierasch *et al.* 1986, Flasar *et al.* 1987, Conrath *et al.* 1991). In each case, thermal wind calculations show zonal wind speeds decreasing with altitude at all latitudes. It is possible that frictional drag on the zonal jets causes them to decay with height. Conrath *et al.* (1990) explored the dynamics of the stratospheres of the giant planets, and found that a key determinant is the ratio of the radiative time scale to the time scale of dynamical friction. When this ratio is large, differential flow is suppressed by friction before radiatively induced temperature differences become large. When the frictional time scale is longer than the radiative relaxation time, radiatively driven differential rotation is not frictionally damped. They found, using a linear radiative–dynamical model, that the tropospheric thermal structure and cloud top winds implied a frictional damping time scale comparable to the radiative relaxation time. Voyager IRIS results show that the ratio of these time scales is of order unity for all of the giant planets, although the reasons behind this are not well understood. The agreement between our derived mean vertical shear in the zonal wind and the Conrath *et al.* (1989) results independently supports this result for Neptune.

Our finding of a slow decay of the winds with height above the cloud deck, coupled with the presumed depth of the circulation below the clouds, implies that the zonal jets are not shallowly confined to the clouds themselves. The strength of the zonal wind and its depth may be related—both imply that dissipation is relatively weak. Interestingly, Hubbard *et al.* (1997) have found similar results for Saturn's stratosphere. By measuring the shape of the limb from multiple atmosphere occultations, they find that Saturn's strong equatorial jet extends essentially undiminished from the cloud deck all the way to the microbar level.

5.2. Neptune's Rotation Figure

Differential rotation at cloud levels is characteristic of all the giant planets, but the decay of winds with height suggests that, at upper levels, the atmosphere eventually reaches uniform rotation. What is the rotation period of this stratospheric rotation? How does it compare to the rotation of the deep interior, and how is it achieved? We can explore these issues using equilibrium theory. The relationship between the solid body rotation frequency Ω and the oblateness ε is, to second order (Zharkov and Trubitsyn 1974),

$$\varepsilon \equiv \frac{r_e - r_p}{r_e} \simeq \frac{1}{2}\left[1 + \frac{3}{2}J_2\left(\frac{r_{ref}}{r_e}\right)^2\right]\left[m + 3J_2\left(\frac{r_{ref}}{r_e}\right)^2\right]$$
$$+ \frac{5}{8}J_4\left(\frac{r_{ref}}{r_e}\right)^4, \tag{13}$$

where r_e and r_p are the equatorial and polar radii, respectively, r_{ref} is the reference radius (25,225 km) for J_2 and J_4, m is defined implicitly by

$$m \equiv \frac{\Omega^2 s^3}{GM_N}$$
$$\simeq \frac{\Omega^2 r_e^3}{GM_N}(1 - \varepsilon), \tag{14}$$

and s is the average radius.

Previous studies have assumed that Neptune's rotation figure is oblate, as one would expect for slow, *uniform* rotation, but Fig. 3 illustrates that Neptune's zonal winds introduce deviations from an approximately elliptical reference geoid computed under the assumption of uniform rotation. In fact, it is precisely these deviations which we have used to determine the differential rotation from the central flash observations. Earlier, we alluded to the fact that a simple oblate limb model could not simultaneously match all three central flash profiles. This is demonstrated in Fig. 13a, where we have plotted χ^2 of separate fits to each occultation as a function of the oblateness of the limb at the $p_{flash} = 0.38$-mbar level. The corresponding rotation period from Eq. (13) is included as the upper x-axis of the plot. We find that the n39 event is best fitted by an oblateness $\varepsilon \simeq 0.021$, in good agreement with the Hubbard *et al.* (1987) determination from fits to the n39 central flash observations of $\varepsilon = 0.0202 \pm 0.0013$, where the latter value has been corrected for the revised value of Neptune's pole direction (Nicholson *et al.* 1995b). However, such a large oblateness produces a very poor match to the N51 central flash, which is best fitted with a limb oblateness of $\varepsilon \simeq 0.017$. There is no single value of ε that produces a good fit to both n39 and N51 central flashes, even though an elliptical model does work for the atmospheric observations at the $p_{1/2}$ level.[8]

From Voyager radio science (RSS) measurements and cloud motions, Lindal *et al.* (1990) found the oblateness of the 1-bar isobaric surface to be $\varepsilon_{1bar} = 0.0171 \pm 0.0014$, with an equatorial radius $r_2 = 24764 \pm 15$ km. Using Eq. (13) the rotation period $P = 2\pi/\Omega$ of a rigid body with this oblateness is $P_{1\,bar} = 16.84^{+1.11}_{-0.93}$ h, consistent with the deep rotation period of 16.11 h found from magnetic field measurements. The oblateness at the p_{flash} level with the RSS rotation period is $\varepsilon = 0.0173$, as plotted in Fig. 13a. Since the depth of the differential zonal flow below the cloud deck is not known, however, the applicability of a uniform rotation model is suspect at this pressure level.

From the central flash results, which are applicable to the millibar regime, we find that although the winds have

---

[8] As before, the N55 central flash is not very sensitive to the assumed limb shape.
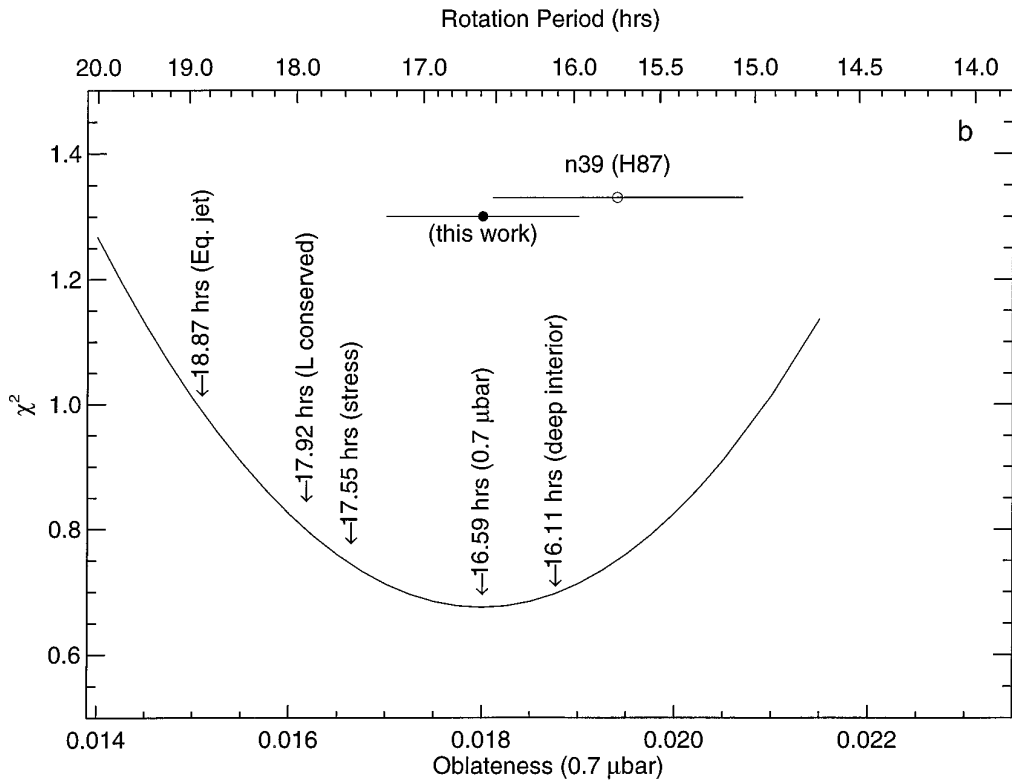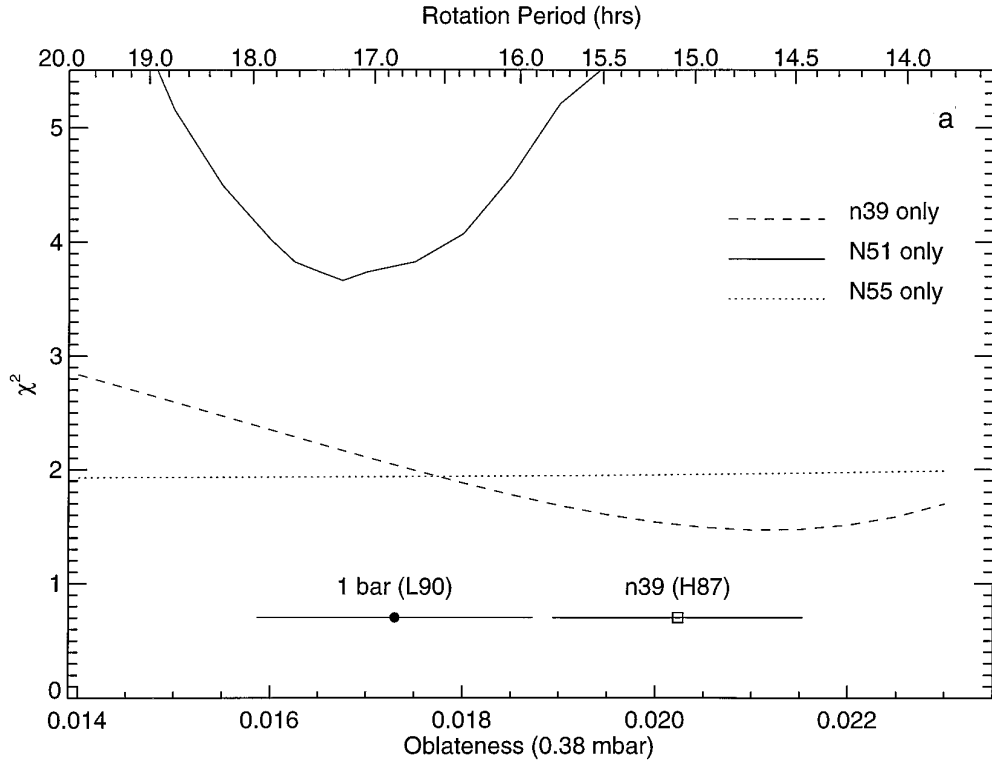
decayed with height, they have not disappeared. On the other hand, the limb fits to the half-light data show that the winds have subsided substantially in the microbar regime. Our formal result ($W = 0.17$) is that the winds have decayed to ~17% of their value at the cloud tops, corresponding to an equatorial rotation period of about 16.52 h, but this assumes that the same shape of the zonal wind profile extends all the way up from the cloud deck to the upper stratosphere. A more secure conclusion is probably that any differential rotation at the $p_{1/2}$ level is very weak. If in actuality there is *no* differential rotation in the upper stratosphere, so that solid body rotation is reached at the microbar level, what is its rotation period compared to the rotation period of the deep interior? To answer this question, we performed a series of fits to the half-light data for a range of assumed limb oblatenesses. The results are shown in Fig. 13b, where we have plotted χ^2 of fits to the atmospheric half-light data as a function of oblateness at the $p_{1/2}$ level and the corresponding rotation period. The best oblate limb fit to the atmosphere data from five occultations (Table I) gives $\varepsilon_{0.7\ \mu bar} = 0.0180 \pm 0.0010$.[9] The corresponding rotation period is $P = 16.59 \pm 0.92$ h, which is quite similar to the deep interior rotation period of 16.11 h. Scaling the formal error in the oblateness to a corresponding formal error in W, we find $\sigma(W) = 0.3$ for the upper stratosphere.

The zonal winds decay with height and converge toward the mean solid body rotation rate characteristic of Neptune's deep interior. What is the mechanism that links the deep rotation of Neptune to the upper stratosphere? The zonal circulation at the cloud levels is primarily retrograde, implying that the bulk of the atmospheric mass is deficient in angular momentum compared to deeper layers. Therefore, if angular momentum were simply redistributed, we

might expect that the upper atmosphere would rotate more slowly than the deep interior. A rigid shell with the same total angular momentum as a differentially rotating shell with a zonal wind profile given by Eq. (3) would have a differential rotation frequency $d\Omega_L$ given by

$$d\Omega_L = \frac{\int_{-\pi/2}^{\pi/2} u_s(\phi) r^3(\phi) \cos^2 \phi \, d\phi}{\int_{-\pi/2}^{\pi/2} r^4(\phi) \cos^3 \phi \, d\phi}, \qquad (15)$$

where

$$r(\phi) = r_e[\cos^2 \phi + \sin^2 \phi/(1 - \varepsilon)^2]^{-1/2}. \qquad (16)$$

Numerically, the corresponding rotation period is 17.92 h, with an ellipticity of $\varepsilon = 0.0162$ at the $p_{1/2} = 0.7$-μbar level. This is a substantially slower rotation period, and lower oblateness, than we infer from the limb fits shown in Fig. 13b. For comparison, we have also plotted the rotation period (18.87 h) of Neptune's 400 m s^{-1} equatorial retrograde jet.

Another possibility is that solid body rotation in the upper stratosphere might be achieved by a viscous stress proportional to the area-weighted differential velocity, such as might arise from breaking of waves propagated upward from much deeper in the atmosphere. A rigid, uniformly rotating shell coupled to the underlying zonal flow by such a velocity-dependent stress would have a differential rotation frequency $d\Omega_{shear}$ given by

$$d\Omega_{shear} = \frac{\int_{-\pi/2}^{\pi/2} u_s(\phi) r^2(\phi) \cos \phi \, d\phi}{\int_{-\pi/2}^{\pi/2} r^3(\phi) \cos^2 \phi \, d\phi}, \qquad (17)$$

with a corresponding rotation period of 17.55 h and an

---

[9] This is close to the Hubbard *et al.* (1987) result of $\varepsilon_{0.7\ \mu bar} = 0.0194 \pm 0.0013$ obtained from fits to the n39 atmosphere data, where we have scaled their value to account for the revised geometry of this occultation.

FIG. 13. (a) Results of a series of fits to each of the three central flash profiles. For each set of fits, χ^2 is plotted as a function of the assumed oblateness of the limb at the $p_{flash} = 0.38$-mbar level (lower axis) and the corresponding rotation period (upper axis). The n39 central flash is best fitted by an oblateness $\varepsilon \simeq 0.021$, close to the Hubbard *et al.* (1987) determination from fits to the n39 central flash observations, labeled as (H87). The N51 central flash requires a much smaller oblateness of $\varepsilon \simeq 0.017$ to give a good match to the data. The N55 central flash is not very sensitive to the assumed planetary shape, since the observer path was so far from the caustic. No single value of the oblateness produces model central flash profiles that match all three lightcurves. The Lindal *et al.* (1990) $p = 1$-bar oblateness measurement, scaled to the $p_{flash} = 0.38$-mbar level, is labeled as (L90). (b) Results of a series of fits to half-light measurements from five occultations, with χ^2 plotted as a function of the assumed oblateness of the limb at the $p_{1/2} = 0.7$-μbar level (lower axis) and the corresponding rotation period (upper axis). Our best fit is for $\varepsilon = 0.0180 \pm 0.0010$, shown as a filled circle. The Hubbard *et al.* (1987) determination from fits to the n39 atmospheric observations is shown as an open circle and labeled as (H87). The oblatenesses corresponding to several rotation periods of interest are marked by arrows. The deep interior rotation period is 16.11 h, close to the 16.59-h period at the $p_{1/2}$ level implied by our best fit. The upper stratosphere seems to be nearly corotating with the deep interior, even though the lower atmosphere has strong retrograde zonal flow. For example the cloud-level equatorial jet has a rotation period of 18.87 h. If the angular momentum of the zonal flow at the $p_{cloud} = 100$-mbar level were redistributed into a uniformly rotating shell, its rotation period would be 17.92 h. If instead, an area-weighted stress proportional to velocity were responsible for the decay of winds with height, the expected uniform rotation period would be 17.55 h.

ellipticity of 0.0166 at the $p_{1/2} = 0.7$-μbar level. Once again, the rotation is slower than implied by our limb fit results.

6. CONCLUSIONS

Neptune's atmosphere has extremely strong differential rotation at the cloud level, but the winds decrease in strength higher in the atmosphere. Voyager IRIS measurements have been used to infer the vertical shear in the zonal wind between the 30- and the 120-mbar level, but it has not been clear at what point in the stratosphere the differential flow would relax to solid body rotation, nor its rotation period compared to the deep rotation of the planet. From our analysis of three central flash observations, we have shown both by scaling the Voyager results and by direct retrieval that the zonal winds at the 0.38-mbar level have subsided to about 60% of their strength at the 100-mbar level. The implied mean vertical shear in the zonal wind over this $\sim 5H$ interval is very similar to that inferred from the IRIS measurements. From fits to atmospheric occultation measurements, we have also determined Neptune's shape at the microbar level. When the upper stratospheric winds in this region are assumed to have the same shape as that just above the clouds, we find that the strength of the zonal flow has decreased to about 17% of the full strength at the 100-mbar level. Alternatively, when we model the limb as an oblate spheroid, we find that the corresponding rotation period for solid body rotation is $\simeq 16.59$ h, very close to the 16.11-h period of Neptune's deep interior.

We are left with a puzzle. Neptune's upper stratosphere seems to corotate with the deep interior of the planet, although there are intervening atmospheric layers containing a great deal of mass that show strong differential rotation and generally retrograde flow. It is almost as though the upper stratosphere were strongly coupled to the planet's magnetic field, but it is difficult to understand how such coupling could take place at regions so far removed from the ionosphere. A more likely explanation is that angular momentum from deeper regions is transported upward and deposited into the upper stratosphere by breaking of inertia–gravity waves, but the details of such a mechanism remain to be explored.

ACKNOWLEDGMENTS

REFERENCES

Baines, K. H., H. B. Hammel, K. A. Rages, P. N. Romani, and R. E. Samuelson 1995. Clouds and hazes in the atmosphere of Neptune. In *Neptune and Triton* (D. P. Cruikshank, Ed.), pp. 109–138. Tucson. Univ. of Arizona Press.

Conrath, B. J., and J. A. Pirraglia 1983. Thermal structure of Saturn from Voyager infrared measurements—Implications for atmospheric dynamics. *Icarus* **53**, 286–292.

Conrath, B. J., F. M. Flasar, and P. J. Gierasch 1991. Thermal structure and dynamics of Neptune's atmosphere from Voyager measurements. *J. Geophys. Res.* **96**, 18,931–18,939.

Conrath, B. J., F. M. Flasar, R. Hanel, V. Kunde, W. Maguire, J. Pearl, J. Pirraglia, R. Samuelson, P. Gierasch, A. Weir, B. Bezard, D. Gautier, D. Cruikshank, L. Horn, R. Springer, and W. Shaffer 1989. Infrared observations of the neptunian system. *Science* **246**, 1454–1459.

Conrath, B. J., P. J. Gierasch, and S. S. Leroy 1990. Temperature and circulation in the stratosphere of the outer planets. *Icarus* **83**, 255–281.

Elliot, J. L., R. G. French, E. Dunham, P. J. Gierasch, J. Veverka, C. Church, and C. Sagan 1977. Occultation of ε Geminorum by Mars. II. The structure and extinction of the martian upper atmosphere. *Astrophys. J.* **217**, 661–679.

Flasar, F. M., B. J. Conrath, J. A. Pirraglia, and P. J. Gierasch 1987. Voyager infrared observations of Uranus' atmosphere—Thermal structure and dynamics. *J. Geophys. Res.* **92**, 15,011–15,018.

Freeman, K. C., and G. Lyngå 1970. Data for Neptune from occultation observations. *Astrophys. J.* **160**, 767–780.

French, R. G., P. A. Melroy, R. L. Baron, E. W. Dunham, and K. J. Meech 1985. The 1983 June 15 occultation by Neptune. II. The oblateness of Neptune. *Astron. J.* **90**, 2624–2638.

French, R. G., P. D. Nicholson, M. L. Cooke, J. L. Elliot, K. Matthews, O. Perkovic, E. Tollestrup, P. Harvey, N. J. Chanover, M. A. Clark, E. W. Dunham, W. Forrest, J. Harrington, J. Pipher, A. Brahic, I. Grenier, F. Roques, and M. Arndt 1993. Geometry of the Saturn system from the 3 July 1989 occultation of 28 Sgr and Voyager observations. *Icarus* **103**, 163–214.

Gierasch, P. J., J. A. Magalhaes, and B. J. Conrath 1986. Zonal mean properties of Jupiter's upper troposphere from Voyager infrared observations. *Icarus* **67**, 456–483.

Hammel, H. B., R. F. Beebe, E. M. De Jong, C. J. Hansen, C. D. Howell, A. P. Ingersoll, T. V. Johnson, S. S. Limaye, J. A. Magalhaes, J. B. Pollack, L. A. Sromovsky, V. E. Suomi, and C. E. Swift 1989. Neptune's wind speeds obtained by tracking clouds in Voyager images. *Science* **245**, 1367–1369.

Hanel, R., B. Conrath, F. M. Flasar, V. Kunde, W. Maguire, J. Pearl, J. Pirraglia, R. Samuelson, L. Herath, and M. Allison 1981. Infrared observations of the saturnian system from Voyager 1. *Science* **212**, 192–200.

Hanel, R., B. J. Conrath, F. M. Flasar, V. Kunde, W. Maguire, J. Pearl, J. Pirraglia, R. Samuelson, D. Cruikshank, and D. Gautier 1982. Infrared observations of the saturnian system from Voyager 2. *Science* **215**, 544–548.

Hanel, R., B. Conrath, F. M. Flasar, V. Kunde, W. Maguire, J. Pearl, J. Pirraglia, R. Samuelson, L. Horn, and P. Schulte 1986. Infrared observations of the uranian system. *Science* **233**, 70–74.

Hubbard, W. B., H. P. Avey, B. Carter, J. Frecker, H. H. Fu, J.-A. Gehrels, T. Gehrels, D. M. Hunten, H. D. Kennedy, L. A. Lebofsky, K. Mottram, T. Murphy, A. Nielsen, A. A. Page, H. J. Reitsema, B. A. Smith, D. J. Tholen, B. Varnes, F. Vilas, M. D. Waterworth, H. H. Wu, and B. Zellner 1985. Results from observations of the 15 June 1983 occultation by the Neptune system. *Astron. J.* **90**, 655–667.

Hubbard, W. B., E. Lellouch, B. Sicardy, A. Brahic, F. Vilas, P. Bouchet, R. A. McLaren, and C. Perrier 1988. Structure of scintillation in Neptune's occultation shadow. *Astrophys. J.* **325**, 490–502.

Hubbard, W. B., P. D. Nicholson, E. Lellouch, B. Sicardy, A. Brahic, F.

Vilas, P. Bouchet, R. A. McLaren, R. L. Millis, L. H. Wasserman, J. H. Elias, K. Matthews, J. D. McGill, and C. Perrier 1987. Oblateness, radius and mean stratospheric temperature of Neptune from the 1985 August 20 occultation. *Icarus* **72,** 635–646.

Hubbard, W. B., C. C. Porco, D. M. Hunten, G. H. Rieke, M. J. Rieke, D. W. McCarthy, V. Haemmerle, J. Haller, B. McLeod, L. A. Lebofsky, R. Marcialis, J. B. Holberg, R. Landau, L. Carrasco, J. Elias, M. W. Buie, E. W. Dunham, S. E. Persson, T. Boroson, S. West, R. G. French, J. Harrington, J. L. Elliot, W. J. Forrest, J. L. Pipher, R. J. Stover, A. Brahic, and I. Grenier 1997. Structure of Saturn's mesophere from the 28 Sgr occultations. *Icarus* **130,** 404–425.

Hubbard, W. B., and 45 colleagues 1993. The occultation of 28 Sgr by Titan. *Astron. Astrophys.* **269,** 541–563.

Ingersoll, A. P. 1990. Atmospheric dynamics of the outer planets. *Science* **248,** 308–315.

Jacobson, R. A., G. D. Lewis, W. M. Owen, J. E. Riedel, D. C. Roth, S. P. Synnott, and A. H. Taylor 1990. Ephemerides of the major neptunian satellites determined from earth-based astrometric and Voyager imaging observations. In *AIAA/AAS Astrodynamics Conference, Portland OR, Aug 20–22, 1990, Technical Papers*. Part 1 (A90-52957 24-13). pp. 157–167. American Institute of Aeronautics and Astronautics, Washington, DC.

Kovalevsky, J., and F. Link 1969. Diamètre, aplatissement et propriétés optiques de la haute atmosphère de Neptune d'après l'occultation de l'étoile BD-17 4388. *Astron. Astrophys.* **2,** 398.

Lellouch, E., W. B. Hubbard, B. Sicardy, F. Vilas, and P. Bouchet 1986. Occultation determination of Neptune's oblateness and stratospheric methane mixing ratio. *Nature* **324,** 227–231.

Limaye, S. S., and L. A. Sromovsky 1991. Winds of Neptune: Voyager observations of cloud motions. *J. Geophys. Res.* **96,** 18,941–18,960.

Lindal, G. F., J. R. Lyons, D. N. Sweetnam, V. R. Eshelman, D. P. Hinson, and G. L. Tyler 1990. The atmosphere of Neptune: Results of radio occultation measurements with the Voyager 2 spacecraft. *Geophys. Res. Lett.* **17,** 1733–1736.

Lindal, G. F., D. N. Sweetnam, and V. R. Eshelman 1985. The atmosphere of Saturn: An analysis of the Voyager radio occultation measurements. *Astron. J.* **90,** 1136–1146.

Mink, D. J., and A. R. Klemola 1985. Predicted occultations by Uranus, Neptune and Pluto: 1985–1990. *Astron. J.* **90,** 1894–1899.

Narayan, R., and W. B. Hubbard 1988. Theory of anisotropic refractive scintillation: Application to stellar occultations by Neptune. *Astrophys. J.* **325,** 503–518.

Nicholson, P. D., C. A. McGhee, and R. G. French 1995a. Saturn's central flash from the 3 July 1989 occultation of 28 Sgr. *Icarus* **113,** 57–83.

Nicholson, P. D., I. Mosqueira, and K. Matthews 1995b. Stellar occultation observations of Neptune's rings: 1984–1988. *Icarus* **113,** 295–330.

Owen, W. M., R. M. Vaughan, and S. P. Synnott 1991. Orbits of the six new satellites of Neptune. *Astron. J.* **101,** 1511–1515.

Roques, F., B. Sicardy, R. G. French, W. B. Hubbard, A. Barucci, P. Bouchet, A. Brahic, J.-A. Gehrels, T. Gehrels, I. Grenier, T. Lebertre, J. Lecacheux, J. P. Maillard, R. A. McLaren, C. Perrier, F. Vilas, and M. D. Waterworth 1994. Neptune's upper stratosphere, 1983–1990: Ground-based stellar occultation observations. III. Temperature profiles. *Astron. Astrophys.* **288,** 985–1011.

Sicardy, B., F. Roques, and A. Brahic 1991. Neptune's rings, 1983–1989: Groundbased stellar occultation observations. I. Ring-like arc detections. *Icarus* **89,** 220–243.

Smith, B. A., L. A. Soderblom, D. Banfield, C. Barnet, A. T. Basilevsky, R. F. Beebe, K. Bollinger, J. M. Boyce, A. Brahic, G. A. Briggs, R. H. Brown, C. Chyba, S. A. Collins, T. Colvin, A. F. Cook II, D. Crisp, S. K. Croft, D. Cruikshank, J. N. Cuzzi, G. E. Danielson, M. E. Davies, E. De Jong, L. Dones, D. Godfrey, J. Gougen, I. Grenier, V. R. Haemmerle, H. Hammel, C. J. Hansen, C. P. Helfenstein, C. Howell, G. E. Hunt, A. P. Ingersoll, T. V. Johnson, J. Kargel, R. Kirk, D. I. Kuehn, S. Limaye, H. Masursky, A. McEwen, D. Morrison, T. Owen, W. Owen, J. B. Pollack, C. C. Porco, K. Rages, P. Rogers, D. Ruby, C. Sagan, J. Schwartz, E. M. Shoemaker, M. Showalter, B. Sicardy, D. Simonelli, J. Spencer, L. A. Sromovsky, C. Stoker, R. G. Strom, V. E. Suomi, S. P. Synnott, R. J. Terrile, P. Thomas, W. R. Thompson, A. Verbiscer, and J. Veverka 1989. Voyager 2 at Neptune: Imaging science results. *Science* **246,** 1422–1454.

Sromovsky, L. A., S. S. Limaye, and P. M. Fry 1993. Dynamics of Neptune's major cloud features. *Icarus* **105,** 110–141.

Standish, E. M., Jr. 1990. The observational basis for JPL's DE 200, the planetary ephemerides of the Astronomical Almanac. *Astron. Astrophys.* **233,** 252–271.

Standish, E. M., Jr., X X Newhall, J. G. Williams, and D. K. Yeomans 1992. Orbital ephemerides of the sun, moon, and planets. In *Explanatory Supplement to the Astronomical Almanac* (P. K. Seidelmann, Ed.), pp. 279–323. U.S. Naval Observatory, Washington, DC.

Warwick, J. W., D. R. Evans, G. R. Peltzer, R. G. Peltzer, J. H. Romig, C. B. Sawyer, A. C. Riddle, A. E. Schweitzer, M. D. Desch, M. L. Kaiser, W. M. Farrell, T. D. Carr, I. de Pater, D. H. Staelin, S. Gulkis, R. L. Poynter, A. Boischot, F. Genova, Y. LeBlanc, A. Lecacheux, B. M. Pedersen, and P. Zarka 1989. Voyager planetary radio astronomy at Neptune. *Science* **246,** 1498–1501.

Zharkov, V. N., and V. P. Trubitsyn 1974. Determination of the equation of state of the molecular envelopes of Jupiter and Saturn from their gravitational moments. *Icarus* **21,** 152–156.